Investigation of Dual Airborne Laser Scanners for Detection and State Estimation of

Mobile Obstacles in an Aircraft External Hazard Monitor

A thesis presented to

the faculty of

the Russ College of Engineering and Technology of Ohio University

In partial fulfillment

of the requirements for the degree

Master of Science

Mark A. Smearcheck

June 2008

This thesis titled

Investigation of Dual Airborne Laser Scanners for Detection and State Estimation of

Mobile Obstacles in an Aircraft External Hazard Monitor

by

MARK A. SMEARCHECK

has been approved for

the School of Electrical Engineering and Computer Science

and the Russ College of Engineering and Technology by

Maarten Uijt de Haag

Associate Professor of Electrical Engineering and Computer Science

---

Dennis Irwin

Dean, Russ College of Engineering and Technology

ABSTRACT

SMEARCHECK, MARK A., M.S., June 2008, Electrical Engineering

<u>Investigation of Dual Airborne Laser Scanners for Detection and State Estimation of</u>

<u>Mobile Obstacles in an Aircraft External Hazard Monitor</u> (124 pp.)

Director of Thesis: Maarten Uijt de Haag

To ensure aircraft safety during precision approach procedures detailed information pertaining to hazards located on the runway and surroundings area must be known. In order to identify possible safety threats, aircraft could be equipped with sensors capable of detecting all significant hazards in a variety of weather conditions and landing scenarios. An analysis of potential hazards and sensor capabilities serves as the basis of this research. One such hazard monitoring implementation is proposed that makes use of two airborne laser scanners, GPS, and an inertial measurement unit. The goal of this implementation is to detect a ground vehicle driving on the runway during aircraft precision approach. Capabilities of the system include accurate geo-referencing of laser footprints, hazard detection and classification, and hazard state estimation. These goals are accomplished with digital surface modeling using sensor and navigation information, a measurement classification method using a windowed weighted least squares algorithm, and unsupervised clustering. Experimental flight-testing has been performed to collect aircraft navigation data, laser measurements of a vehicle in motion on the runway, and vehicle position truth data. Results indicate geo-referencing accuracy of approximately 2 m in most cases, along with successful hazard classification, and hazard velocity estimates accurate to within 2.8 m/s.

Approved: _____

Maarten Uijt de Haag

Associate Professor of Electrical Engineering and Computer Science

ACKNOWLEDGMENTS

First I would like to thank my advisor, Dr. Maarten Uijt de Haag, for the continued guidance, support, and friendship he has provided me during this research and my time at Ohio University. Since early in my undergraduate career Dr. Uijt de Haag has always supplied me with motivation and new challenges, while making sure that I learned as much as possible along the way. I would also like to thank my other committee members, Dr. Frank van Graas and Dr. Jeff Dill. Flight-testing and data collection could not have been accomplished without the help of both Dr. Uijt de Haag and Dr. van Graas.

Next I would like to thank Ananth Vadlamani for all of the assistance he has provided me. This research may not have gotten off the ground if it were not for a conversation held between Ananth and I at a restaurant in St. Louis while passing the time before a flight. His countless ideas and suggestions along with his willingness to spend hours helping me debug MATLAB code are greatly appreciated.

I would like to thank my officemate, roommate, and friend, Don Venable. We have been working together and bouncing ideas off of each other for the past seven years and hopefully will continue to do so for years to come. Some of the algorithms implemented in this research have a foundation in previous works of his. I also thank Kyle Venable for assisting with the background chapter of my thesis.

TABLE OF CONTENTS

LIST OF TABLES

LIST OF FIGURES

Page

LIST OF ACRONYMS

ADS-B	Automatic Dependent Surveillance-Broadcast
ALS	Airborne Laser Scanner
AMASS	Airport Movement Area Safety System
ASDE	Airport Surface Detection Equipment
CCD	Charge Coupled Device
CFIT	Controlled Flight into Terrain
DCM	Direction Cosine Matrix
DGPS	Differential GPS
DTM	Digital Terrain Model
DSM	Digital Surface Model
ECEF	Earth-Centered Earth Fixed
ENU	East-North-Up
EVS	Enhanced Vision System
FAA	Federal Flight Administration
FLIR	Forward Looking Infrared
GPS	Global Positioning System
IIFD	Intelligent Integrated Flight Deck
IMU	Inertial Measurement Unit
IR	Infrared
LADAR	Laser Radar
LIDAR	Light Detection and Ranging
LWIR	Long Wave Infrared
MMWR	Millimeter Wave Radar
NASA	National Aeronautics and Space Agency
NED	North-East-Down
NGATS	Next Generation Air Transportation System
NTSB	National Transportation Safety Board
RF	Radio Frequency
RGB	Red Green Blue
RIPS	Runway Incursion Prevention System
RLG	Ring Laser Gyro
SAR	Synthetic Aperture Radar
SIFT	Scale-invariant Feature Transform
SLAM	Simultaneous Localization and Mapping
SVS	Synthetic Vision System
SWIR	Shortwave Infrared
TCAS	Traffic Collision Avoidance System
UV	Ultraviolet
VDL	Very High Frequency Data Link
WAAS	Wide Area Augmentation System
WxR	Weather Radar

CHAPTER 1: INTRODUCTION

1.1 Problem Statement

During aircraft precision approach pilots are faced with the danger of having limited or zero knowledge of hazards located on or near the runway that may interfere with safe landing operations. Obstacles posing a potential threat to safety include ground vehicles, other aircraft, pedestrians, wildlife, buildings and towers, signs and markers, debris, and even weather. The location and possibly the existence of these hazards are often unknown, resulting in reduced pilot situation awareness and an increase in the likelihood of aircraft to hazard collisions.

Current systems such as Automatic Dependent Surveillance-Broadcast (ADS-B) [1], Traffic Collision Avoidance System (TCAS) [2], and Airport Movement Area Safety System (AMASS) [3], have been developed to provide limited hazard alerting. These technologies rely on systems external to the aircraft to supply information to the pilot pertaining to the location of other cooperative aircraft and vehicles that are similarly equipped with this system. With the exception of the ground radar based AMASS, the aforementioned hazard alerting techniques contribute to landing safety by identifying threats posed by participants in the alerting system, though they do not incorporate non-cooperative hazards that lack alerting devices. The absence of non-cooperative hazard identification is a severe limitation to the safety systems. Knowledge of stationary hazards such as buildings, towers, signs and markers, and possibly foliage may reside in

an onboard database; however, the location and state of hazards such as pedestrians, wildlife, construction equipment, debris, and possibly vehicles are unknown to each of these systems. A method for detecting, classifying, and estimating the state of all possible hazards is required to ensure complete runway safety.

The National Aeronautics and Space Administration (NASA) has acknowledged the problem of runway hazard detection and made it a key component of the Next Generation Air Transportation System (NGATS), a system designed to improve flight robustness, management, and safety through advanced automation, sensing, and communication [4]. Hazard detection in the NASA concept of NGATS will be realized via the Intelligent Integrated Flight Deck (IIFD), a flight deck containing displays capable of providing vast amount of flight critical information to the pilot in an efficient and effective manner. Much of this flight critical information will come from sensors internal to the aircraft.

For detection, classification, and state estimation of hazards to prove successful the system must first have detailed knowledge of the types of objects that may serve as hazards. This knowledge includes physical properties such as size, shape, motion, cooperation, and threat level. Once the hazards and their properties are defined, an appropriate sensor suite can be selected that detects all potential hazards, takes advantage of the hazard properties, and performs effectively in a multitude of weather conditions.

This work is an investigation into one such sensing suite and is performed in conjunction with NASA's NGATS research. Light detection and ranging (LIDAR) coupled with a precise navigation solution is utilized for detection and tracking of vehicles in motion on the runway and nearby airport surfaces, which may become a potential threat to aircraft landing safety.

1.2 Proposed Solution

Mobile hazards are identified and classified using measurements from dual airborne laser scanners (ALS) and aircraft navigation systems. The laser footprints are first geo-referenced by use of direction cosine matrices (DCMs) for coordinate system transformation and rotation, accurate instrument and sensor lever-arm measurements, and kinematic differential Global Positioning System (DGPS) data. The accuracy of these measurements is determined by use of truth data acquired from a (Global Positioning System) GPS receiver onboard the hazard vehicle and comparison of geo-location results between ALSs using a similar point on the runway determined by the laser intensity values. Laser measurement points are classified as terrain or non-terrain using a windowed weighted least squares method that examines residuals calculated by fitting a plane through a small window of 3-D point cloud data. All non-terrain points are grouped into clusters representing potential hazards using the *k*-means clustering algorithm. Finally the hazard states are estimated by determining the velocity of the hazard through use of geo-referenced information from both ALSs. Note that in an operational

environment, the ALS systems would have to point forward to cover the runway and anticipate the hazards, instead of pointing only slightly forward and downward.

1.3 Contributions

Portions of this research have been previously presented and discussed in various conference papers and were written in conjunction with the research performed for this thesis. A majority of Sections 2.1, 2.3, and 2.4 of this thesis appear in the following publication:

M. Smearcheck, A. Vadlamani, and M. Uijt de Haag, "Sensor classification and obstacle detection for aircraft external hazard monitoring," in *Proceedings of SPIE Vol. 6957, Enhanced and Synthetic Vision 2008*, 2008. [5]

The foundation for ALS hazard detection used in this thesis was previously discussed in the following publication.

A. Vadlamani, M. Smearcheck, M. Uijt de Haag, "Preliminary design and analysis of a LIDAR based obstacle detection system," in *Proceedings of The 24th Digital Avionics Systems Conference*, 2005, pp. 6.B.2-61-14. [6]

Ideas presented by authors of the following papers have also served as a basis for this work.

A. Vadlamani and M. Uijt de Haag, "Arial vehicle navigation over unknown terrain using inertial measurements and dual airborne laser scanners or flash ladar," in *Proceedings of SPIE Vol. 6550, Laser Radar Technology and Applications XII*, 2007. [7]

D. Venable, J. Campbell, and M. Uijt de Haag, "Feature extraction and separation in airborne laser scanner terrain integrity monitors," in *Proceedings of The 24th Digital Avionics Systems Conference*, 2005, pp. 4.E.3-41-11. [8]

1.4 Overview of Thesis

This thesis is arranged into six chapters. Chapter 1, the introduction, presents the problem and proposed solution along with a discussion of contributions to this work. The next two chapters provide background and mathematical theory used to support the proposed method of hazard detection and tracking. Landing safety statistics, particulars of runway hazards, classification of aircraft sensors, current hazard alerting systems, and ongoing research in this area are discussed as the background in Chapter 2. Chapter 3 presents the mathematically theory; specifically techniques for geo-referencing of the LIDAR data, object detection using LIDAR, and state estimation. The experimental methodology including specifics of sensors, navigation instruments, the ground vehicle hazard, the data collection procedure, and detection algorithms is explained in Chapter 4. Detailed results

of the proposed solution are presented in Chapter 5. Finally, Chapter 6 provides

conclusions and discusses challenges and suggestions for future research in this area.

CHAPTER 2: BACKGROUND

2.1 Runway Safety

Risk is always involved during aircraft operations on or in the vicinity of the runway. The potential for collisions with nearby aircraft, ground vehicles, pedestrians, wildlife, buildings, debris, and other hazards poses a significant threat to safety. The realization of such risk during takeoff, taxiing, and landing is classified as a runway incursion. The Federal Aviation Administration (FAA) defines a runway incursion as "*any occurrence in the airport runway environment involving an aircraft, vehicle, person, or object on the ground that creates a collision hazard or results in a loss of required separation with an aircraft taking off, intending to take off, landing, or intending to land* [9][10]." Runway incursions are divided into separate categories based on the cause and severity of the incident. The categories of incursion severity along with their recent occurrence rates are provided in Table 2.1.

Table 2.1

Severity Categories of Runway Incursions [9]

Incursion Category	Description	Number of Occurrences 2003 - 2006
D	Little or no chance of collision but meets the definition of a runway incursion.	768
C	Separation decreases but there is ample time and distance to avoid a potential collision.	400
B	Separation decreases and there is a significant potential for a collision.	60
A	Separation decreases and participants take extreme action to narrowly avoid a collision, or the event results in a collision.	60

With nearly 1280 runway incursions occurring over a four year period, as shown in Table 2.1, it is clear that further safety measures must be put into place to avoid dangerous and possibly fatal situations. Before new safety systems can be implemented, the various causes of aircraft to hazard collisions and near-collisions must be examined. The FAA has designated three primary factors as key attributers to runway incursions [11].

- Operational errors and deviations

- Pilot deviations

- Vehicle and pedestrian deviations

Operational errors and deviations can be mainly attributed to air traffic control (ATC); an air traffic controller directs the aircraft into a previously occupied area. Insufficient air traffic controller tower height and lack of radar surveillance in some airports can cause

controllers to completely lose visual contact with ground traffic resulting in operational

"lack of situational awareness" and deviations [11]. A hazard detection system internal to

the aircraft could reduce these incidences by providing an immediate warning to the

flight crew, regardless of the instructions of the air traffic controller. Pilot deviations

caused by noncompliance with FAA regulations such as hold commands and lack of

authorization to enter an area of the runway or taxiway also lead to severe incursions,

potentially causing a collision with another aircraft [9]. The final factor attributing to

runway incursions involves vehicle and pedestrian deviations. Vehicles and pedestrians

entering the runway without proper ATC authorization immediately become hazards

interfering with safe aircraft operations [10]. Insufficient security, absence of signs and

markers, and easy access to surrounding roads is often the cause of pedestrians and

vehicles unknowingly entering runways, taxiways, and the surrounding area [11]. Table

2.2, provided by an FAA Runway Safety Report, is a summary of causes of runway

incursions from 2003-2006.

Table 2.2

Breakdown of Runway Incursions by Deviation Type [9]

Deviation	Total Deviations 2003-2006
Pilot Deviation	706
Operational Errors/Deviations	380
Vehicle Errors/Deviations	220

Organizations responsible for maintaining and improving runway safety such as the

National Transportation Safety Board (NTSB), the FAA, and NASA are aware of the

current safety risks created by objects unknowingly entering the airport movement areas.

The NTSB has made the design of a direct notification system for pilots, warning of

runway hazards and incursions, a primary objective in their "Most Wanted Safety

Improvements" plan for 2007 [12]. NASA and the FAA also have similar intentions with

the development of the IIFD [4].

2.2 Runway Safety Technologies

Multiple runway safety and monitoring systems are currently in place or under

development to help prevent runway incursions. The Runways Incursion Prevention

System (RIPS) makes use of ADS-B to broadcast ownship information, provided by GPS

possibly often supplemented by other systems such as the Local Area Augmentation

System (LAAS) and inertial data, to all other vehicles in the area equipped with an ADS-

B transponder. [13] suggests using only raw GPS measurements (i.e. psuedoranges) for

positioning in ADS-B to allow for aircraft and vehicles that are not capable of making

LAAS or differential based GPS measurements to participate in the system. A backup to

GPS that currently must be considered is eLoran. The transponders receive updates on the

positions of other system participants via a data link such as the very high frequency data

link (VDL)-Mode 2. Traffic information from ADS-B is provided to the pilot on an

electronic moving map display located in the flight deck [1]. RIPS relies on ground

surveillance radar such as the third generation Airport Surface Detection Equipment

(ASDE-3) to detect objects on runway surfaces. This radar system is capable of detecting

large targets with a cross section greater than 3 m^2 at a range resolution of 40 ft and an

azimuth resolution of 80 ft. ASDE-3's radars are located on ATC towers and can be

placed at a height of 50 ft to 300 ft [17].

Another system that makes use of ground surveillance systems, is the Airport Movement

Area Safety System, AMASS. Similar to RIPS, AMASS uses ASDE-3 radar technology

to provide potential runway collision information, however, this information is displayed

to the controller, who is then required to resolve the collision and provide pilots of the

incoming aircraft with warnings [3]. The drawback of indirect communication between

AMASS and pilots causes significant delay and though it was declared fit to detect

runway collisions by he NTSB, it was deemed unfit to detect runway incursions [16].

Less common runway safety systems include Inductive Loop Technology and the

PathProx System. Inductive Loop Technology relies on the placement of sensors inside

the runway surface to detect and classify aircraft and ground vehicles. Loop sensors

generate unique inductive signals based on weight and movement signatures as objects

pass over wire loops embedded in airport surfaces. This information is then relayed

though a wired data link to ATC where it is shown on continuously updating displays

[18]. Advantages of such a system include the ability to detect vehicles located in

surveillance blind spots that are not covered by radar systems such as ASDE-3,

independence of interference susceptible radio frequency (RF) communication, the ability

to classify vehicles and aircraft, and the capability to track these objects. Another alternative runway safety monitor is PathProx developed by the Rannoch Corporation. Similar to RIPS, PathPox relies on ADS-B to acquire positions of other aircraft in the area. It makes use of GPS to determine ownship information. Data from the PathProx system is sent to the aircraft and made available to the pilot in real time on a flight deck display [19].

2.3 Runway Hazards

A prerequisite for the detection of obstacles on the runway is a general understanding of the types and characteristics of hazards an aircraft may encounter. Without this knowledge, selection of an appropriate onboard sensor or sensors is difficult. Key hazard characteristics such as size, shape, velocity, reflectivity, and thermal signature lend themselves better to specific sensors. Designation of a runway hazard is not straightforward in all cases. Factors such as the aircraft operation [14] and potential risk presented by the object influence the classification and severity of an object as a collision hazard. One such example of objects becoming hazards in varying scenarios involves controlled flight into terrain (CFIT), in which the flight crew unknowingly flies into an obstacle or terrain. In this case, all ground features become hazards as opposed to standard operating conditions where only obstacles on or near the approach vector and touchdown area serve as hazards.

Since all hazards cannot be defined in the same manner and often do not share similar

properties, potential hazards have been broken down into three unique categories.

Included in the list of hazard categories are stationary hazards, mobile hazards, and

weather and environmental hazards.

Stationary hazards are comprised of objects such as buildings, trees, and terrain.

Identification of stationary hazards is often easier than identifying mobile objects,

weather, and environmental hazards because once they have been detected their location

can be stored in database similar to those used in synthetic vision systems (SVS) [15] or

relayed to ATC. While collision with a stationary object is an unlikely scenario, it is still

of concern. Listed in Table 2.3 are some of the most safety critical stationary hazards.

Table 2.3

Identification of Important Stationary Safety Hazards

Stationary Hazards	
Towers	Signs and Markers
Buildings	Terrain
Construction Equipment	Foliage
Power Lines	Foreign Object Debris
Closed Runway	Water

As evident from the table above, many stationary hazards have similar physical characteristics. Man-made stationary hazards such as buildings, towers, construction equipment, and signs and markers are highly reflective and their thermal signature varies with the temperature of the environment. Terrain and foliage can be classified as stationary objects that share similar properties. These objects possess low reflectivity values and often contain large amounts of sloped and jagged edges leading to scattered signal returns. For all of the similar properties that are a part of the stationary hazard list, size is not one of them. While large hazards such as buildings are simple to detect with almost any sensor, power lines, foreign object debris, and signs will likely be small and cannot be detected by low-resolution sensors.

The complexity of identifying objects as hazards can be inferred from Table 2.3. Even stationary hazards have specific properties that vary from one object to the next. This makes selection of a single sensor capable of detecting all of these objects difficult. The detection of mobile obstacles is even more challenging since the obstacle sensing equipment must now be able to determine if an object is moving, requiring a significant amount of additional processing equipment. In order to track an object the detection system must be able to resolve the object's velocity and attitude information from the sensor. This would require the sensor to have a built-in capability to determine velocity and attitude accurately and would likely rely on information from the aircraft's navigation instruments. The mobile hazard list in Table 2.4 presents common mobile runway hazards along with typical maximum velocities that the hazards may achieve.

Table 2.4

Identification of Dynamic runway hazards

Mobile Hazards	
Hazard	**Estimated Maximum Speed (km/h)**
Aircraft	300 km/h
Ground Vehicle	70 km/h
Wildlife	25 km/h
Pedestrian	12 km/h

While much work has been conducted for the detection of aircraft through systems such as ADS-B, ASDE, and TCAS [1][17][20], few studies have been conducted for other mobile hazards. Ground vehicles including baggage carts and snow plows are not equipped with instruments to allow them to participate in ADS-B making them currently unmonitored hazards. While the dangers created by avian life have been studied [21], few solutions exist to detect wildlife and pedestrians on or near runway surfaces. As with any living hazard, a detection system involving a sensitive enough infrared (IR) may provide a simple solution under the right weather conditions.

The third category of runway hazards is comprised of weather conditions within the environment along the aircraft path. For precision approach procedures, the weather conditions determine the visibility conditions at the decision height and thus the aircraft

approach Category (I, II, IIIa, b, c) [59]. These conditions, therefore, drive the equipment

that must be onboard the aircraft to proceed with the landing at the decision height.

During en-route procedures, weather conditions may directly affect the safety of the

aircraft if not avoided. In case of weather avoidance, a precise location of the weather

itself may be useful to minimize the impact of the weather on aircraft operations. Table

2.5 presents a list of common weather and environmental hazards posing a risk to flight

safety.

Table 2.5

Identification of Weather and Environmental Hazards

Weather and Environmental Hazards	
Rain	Wake Vortex
Snow	Volcanic Ash
Fog	Wind Shear
Ice	Darkness

2.4 Sensor Characteristics and Applications

Selection of an appropriate sensor or set of sensors for airborne hazard detection and state

estimation, must be driven by both the properties of the hazards and the performance

characteristics of the sensors. This section provides an overview of potential sensors

suitable to detect obstacles in the case of a hazard monitor by examining various

capabilities of sensors in addition to a discussion of current research efforts that make use of these devices.

2.4.1 Forward-Looking Infrared

The first sensing technology to be examined is forward-looking infrared (FLIR), a passive sensor used to determine the relative temperature of objects in a scene [22]. Various IR frequencies lend themselves to specific applications. For instance, shortwave infrared (SWIR), operating at wavelengths of 1.4 μm to 3 μm, is most effective for sensing runway lighting and performs well in fog [23]. Long wave infrared (LWIR) is useful for providing a thermal image of a scene and distinguishing objects from the background. It performs well in low visibility scenarios and can often detect partially hidden targets [24].

FLIR has been used extensively for vision and object detection and tracking in area of avionics and has applications wherever thermal radiance of objects and environments can be used. Current aircraft may be equipped with a synthetic vision system (SVS) or enhanced vision system (EVS) [25] [26] consisting of a visible light, LWIR, and/or SWIR cameras. Methods for detection and tracking include the use of techniques such as fuzzy clustering [27] and Bayesian based jump-diffusion [28]. In addition to airborne applications IR has found its way into surveillance in the areas of pedestrian and vehicle tracking. Further information on current FLIR research can be found in Table A.1 located in Appendix A of this document.

2.4.2 Millimeter Wave Radar

Another airborne sensor that has proven effective for object detection is millimeter wave

radar (MMWR). Operating in the range from 40 GHz to 300 GHz, with optimal

frequencies of 35 GHz, 95 GHz, 140 GHz, and 220 GHz, MMWR can provide images of

moderate resolution in a variety of weather and environmental conditions [29]. In

addition to being a somewhat weather invariant system, partial penetration of objects

such as foliage is possible [30]. Both active and passive MMWRs exist, however, the

latter is prevalent among airborne sensors and relies on the blackbody radiation produced

by the objects. Applications of MMWR include detection of roads and vehicles [30],

targets blocked by foliage [30], power lines [33], and even airborne particles such as

chemicals or moisture [32] [34]. MMWR have also been evaluated for use in SVS and

especially, EVS systems. Table A.2 of Appendix A provides an in-depth look at current

research in the area of millimeter wave imaging.

2.4.3 Vision Cameras

Another proven and well-researched sensing technology is the use of vision cameras.

Operating in the visible light band of the electromagnetic spectrum, these cameras have

been used extensively in the areas of surveillance, mapping, navigation, and tracking.

Performance of traditional vision systems often decreases in the presence of weather and

is unusable in low and zero light scenarios. Fusion of such cameras with sensors and

instruments such as LIDAR [35], ultraviolet (UV) [36], IR [37], and other multispectral

and hyper spectral devices can be used to compensate for environmental factors. For navigation and guidance applications a stereo pair of vision cameras can be used to provide range information [38]. Algorithms such as simultaneous localization and mapping (SLAM) [39], used for navigation, and scale-invariant feature transform (SIFT) [40], often used for tracking, have proven effective and lend themselves well to aircraft external hazard monitors. Current research applicable to hazard monitoring and navigation is examined in Table A.3 of Appendix A.

2.4.4 Flash LIDAR

3-D ranging cameras, often known as Flash LIDAR, are an emerging sensing technology that has shown promise in the areas of facial recognition, navigation, and tracking. Flash LIDAR operates on the principle of detection of a pulsed or modulated laser signal via a focal plane array (FPA). Making use of time-of-flight measurements from a pulsed laser, a 3-D range image of a scene (which can easily be converted to a 3D point cloud) can be captured at rates of up to 30 Hz and resolutions upwards of 150 by 150 pixels. Ranging information provided by these devices is extremely precise, with a depth accuracy of better than 20 mm [41]. Low cost 3-D range cameras have proven a viable option for indoor navigation and machine vision [42] while offering a non-ambiguity range on the order of five to ten meters [41]. Current research into uses of such cameras includes IMU drift compensation using flash LIDAR for navigation [43], terrain mapping [44], and autonomous spacecraft rendezvous and docking [45]. Further applications and additional

flash LIDAR research efforts are provided in Table A.4 of Appendix A. As the resolution and range of these sensors increase, they become more viable options for hazard airborne monitoring solutions. The objectives of the research presented in this thesis could be achieved using a long range, high-resolution 3-D imager. Currently, sensors like these are available but are very costly. For example, Advanced Scientific Concepts does sell a sensor with a range up to 5000 ft, a resolution of 128x128, and a field of view of 9°. An advantage of laser imaging as opposed to current laser scanning techniques is the fact that all range measurements in one frame correspond to the same time epoch and the fact that multiple observations can be made of the same object enabling the estimation of motion from a sequence of images

2.4.5 Airborne Laser Scanner

Airborne laser scanning, a sensing method employing time-of-flight information from a short wave laser, is used to make range measurements to distant objects such as terrain and targets. The ALS scanning mechanism, typically a rotating polygon mirror, allows for a linear sweep pattern of the laser with measurements being made at increments as small as 0.001°. High measurement rates in excess of 100 kHz lead to the creation of high point density maps that have range accuracies at the sub-centimeter level [67]. Traditional long range LIDAR systems have the advantage over vision and FLIR sensors in that they not only yield 3-D data, but are less vulnerable to the amount of background light and/or temperature of the surrounding environment. Some ALS systems possess the

capability to measure the returned amplitude (or intensity) of the laser pulses, resulting in

a non-equidistant gridded IR image and thus providing clues to the types of surfaces that

are being scanned. Advanced ALS sensor models are furthermore capable of returning

multiple pulse echoes from a single scan point, yielding information regarding the bare

Earth, foliages, and possible obstacles. A drawback of ALS is its susceptibility to dense

fog and other high precipitation scenarios [46], however, research is underway to design

LIDAR sensors capable of handling such conditions [47].

Current uses of ALS include map building, surveillance, vehicle and pedestrian

detection, vegetation measurement, weather and particle detection, spacecraft landing,

and aircraft and indoor navigation. Digital terrain models (DTM), accurately depicting

topographic information of an area in the form of a digital bare Earth model are often

constructed by remote sensing techniques such as LIDAR. First a digital surface model

(DSM) containing terrain plus non-terrain features is formed and these features are

subsequently removed using filtering techniques such as the ones found in [48] and [49].

Surveillance applications of LIDAR are broad in scope. Traffic monitoring [50], forest

fire sensing [51], and target detection, similar to the concept being proposed in this

research, are all topics of current interest. Investigations into using ALS for navigation

purposes are also being preformed. The dual LIDAR based hazard monitor concept

presented in this thesis is intended to serve as an extension of a dead-reckoning

navigation system employing dual ALS sensors and an IMU. In this system, a forward-

looking ALS scans the ground in an unknown environment to build a map of the terrain.

A downward looking ALS then scans that same region of terrain and uses the measurement differences to correct for drift errors present in the IMU [7]. The integration of LIDAR with an IMU is used for indoor navigation of autonomous robots. [53] uses a Kalman filtering solution to estimate velocity and heading information, while making use of wall corners as points of interest to determine lateral position inside a hallway. Appendix A, Table A.5 provides further discussion of ALS research topics.

2.4.6 Sensor Assessment

Presented in this section are the physical characteristics and limitations of various sensors that could be integrated into an aircraft external hazard monitor. The parameters and specifications presented in Table 2.6 are based on state of the art commercially available sensors, however, devices with increased capabilities that are in early research and development stages may exist.

Table 2.6

Sensor Characteristics and Specifications for Potential Use in an Aircraft External Hazard Monitor

Sensor	Measurement Type	Spectral Range	Range	Typical Image Resolution	Scan Rate	Scan Width	Field of View	Source
Airborne Laser Scanner	Azimuth, Range, Intensity	0.75 μm to 1.4 μm	500 m to 1.8 km	NA	160 Hz	2.5° to 60°	0.06° to 0.17° (Single Pulse)	[54]
Flash LIDAR	Azimuth, Elevation, Range, Intensity	850 nm	9 m to 1.5 km	128x128	10 Hz	NA	1° to 9°	[55]
Vision Camera	Azimuth, Elevation, Red, Green, Blue	400 nm to 700 nm	NA	1024x1024	7 Hz to 120 Hz	NA	Varies	[56]
FLIR	Azimuth, Elevation, Temperature	750 nm to 1 nm	NA	720x756, 648x486	50 Hz to 60 Hz	NA	Varies	[57]
Millimeter Wave Radar	Azimuth, Elevation, Intensity	35 GHz, 77 GHz, 94 GHz	12 km	NA	$\dfrac{120°}{sec}$	180°	0.1° (Instantaneous)	[58]

A factor that has not been previously discussed but provides a major source of background noise is sunlight. Vision and IR systems, and potentially flash LIDAR, all suffer from the effects of sunlight. Images appear washed out when they are over saturated, making features difficult to detect and distinguish from background in the presence of too much light. Now that sensor characteristics and properties have been examined along with current research into applications of these devices, an assessment can be made, using the knowledge from Section 2.3, on which sensors are capable of detecting particular hazards. Represented in Table 2.7 is a matrix of sensor / hazard capabilities. It should be noted that as sensor technology advances their capabilities to detect the hazards listed in this table will likely increase.

Table 2.7

Hazards Detectable with Specific Sensors [26][29][31][33][34][40][44][49]

Hazard	MMWR	ALS	Flash LIDAR	FLIR	Vision	WxR
Towers	X	X	X	X	X	
Buildings	X	X	X	X	X	
Construction Equipment	X	X	X	X	X	
Power Lines	X					
Runway	X	X	X	X	X	
Foreign Object Debris	X	X	X	X	X	
Signs and Markers	X	X	X	X	X	
Terrain		X	X	X	X	X
Trees / Foliage	X	X	X		X	
Aircraft	X	X	X	X	X	
Ground Vehicle	X	X	X	X	X	
Significant Wildlife		X	X	X	X	
Pedestrians		X	X	X	X	
Ice		X				X
Snow					X	X
Rain					X	X
Fog					X	X
Wake Vortex		X				
Volcanic Ash					X	
Wind Shear		X				X

Based on the information presented in this chapter, LIDAR appears to be an appropriate

sensor for vehicle detection in an aircraft hazard monitoring system. The ability to

produce high resolution and extremely accurate 3-D scene representations in a variety of

environmental conditions makes it a viable solution. Integrating measurements from a

dual ALS implementation provides an increased ability to detect the same target multiple

times, adding a rudimentary capability for tracking. The amplitude of the reflected laser

pulses, correlated to material of a target, may provide further scene information. The next chapter will provide the necessary background to perform the hazard detection and geo-referencing operations.

CHAPTER 3: THEORY

3.1 Theoretical Applications

In order to detect, geo-reference, and estimate the velocity of a hazard in LIDAR data the information presented in this chapter is necessary to provide a basic understanding of the mathematical techniques used in the processes. Coordinate frame transformation and rotation along with linear interpolation are required for LIDAR footprint geo-referencing. Plane fitting in three dimensions, the weighted least squares method, and k-means clustering are used in hazard detection.

3.2 Coordinate Frame Transformation and Rotation

Rotation from one coordinate frame to another is accomplished though the use of direction cosine matrices (DCM). The transformation from ALS range and angle measurements to geo-referenced laser footprints, used in this research to extract objects of interest, requires various coordinate frame rotations. The method for rotation from the aircraft body frame to the navigation frame and the rotation from the navigation frame to the Earth frame are presented in this section.

The body frame of an aircraft is defined as a right-handed coordinate system in which all axes are orthogonal. The positive x-axis extends from the origin, the center of mass of the aircraft, out through the nose of the aircraft. The positive y-axis is defined out of the right wing and the positive z-axis is pointed down. The navigation frame is a local-level frame

with the origin residing at the center of the navigation instrument or instruments. Similar to the z-axis of the body frame, the positive z-axis of the navigation frame also points directly down. The positive x-axis points north and the positive y-axis points east [52].

Three successive rotations are required to construct a DCM used to rotate from one coordinate frame to the other. In the case of a body frame to navigation frame rotation, a rotation must first be performed about the yaw angle, ψ (z-axis), followed by a rotation about the pitch angle, θ (y-axis), and finally about the roll angle, ϕ (x-axis). The product of these three rotations is known as a DCM, which can be used for coordinate frame rotation about a single axis. This nine-element square matrix is used in the body-to-navigation frame rotation. The derivation of each successive rotation is detailed in Equation 3.1 through Equation 3.5 [52].

The first rotation about the z-axis, shown in Figure 3.1, is composed of the following x and y components.
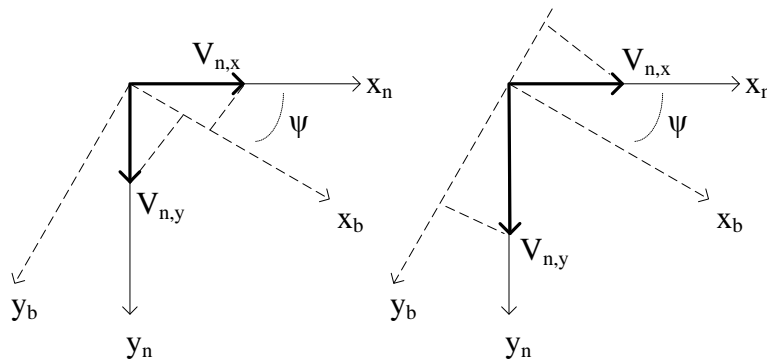
Figure 3.1: Rotation about the z-axis in the body frame to navigation frame rotation

$$v_{b,x} = v_{n,x} \cos\psi + v_{n,x} \sin\psi \qquad (3.1)$$

$$v_{b,y} = -v_{n,y} \sin\psi + v_{n,y} \cos\psi \qquad (3.2)$$

The formation of Equation 3.1 and Equation 3.2 into a matrix forms the yaw angle

rotation as shown in Equation 3.3

$$\begin{bmatrix} v_{b,x} \\ v_{b,y} \\ v_{b,z} \end{bmatrix} = \begin{bmatrix} \cos\psi & \sin\psi & 0 \\ -\sin\psi & \cos\psi & 0 \\ 0 & 0 & 1 \end{bmatrix} \begin{bmatrix} v_{n,x} \\ v_{n,y} \\ v_{n,z} \end{bmatrix} \qquad (3.3)$$

The equivalent rotations about the pitch and roll angles are derived in a manner similar to

the yaw angle rotation, and are defined respectively as

$$\begin{bmatrix} v_{b,x} \\ v_{b,y} \\ v_{b,z} \end{bmatrix} = \begin{bmatrix} \cos\theta & 0 & \sin\theta \\ 0 & 1 & 0 \\ \sin\theta & 0 & \cos\theta \end{bmatrix} \begin{bmatrix} v_{n,x} \\ v_{n,y} \\ v_{n,z} \end{bmatrix} \qquad (3.4)$$

$$\begin{bmatrix} v_{b,x} \\ v_{b,y} \\ v_{b,z} \end{bmatrix} = \begin{bmatrix} 1 & 0 & 0 \\ 0 & \cos\phi & -\sin\phi \\ 0 & \sin\phi & \cos\phi \end{bmatrix} \begin{bmatrix} v_{n,x} \\ v_{n,y} \\ v_{n,z} \end{bmatrix} \qquad (3.5)$$

The body frame to navigation frame DCM of Equation 3.6 can be expressed as a product of the rotations in Equation 3.3 through Equation 3.5

$$\mathbf{C_b^n} = \begin{vmatrix} \cos\theta\cos\psi & -\cos\theta\sin\psi + \sin\phi\sin\theta\cos\psi & \sin\phi\sin\psi + \cos\phi\sin\theta\cos\psi \\ \cos\theta\sin\psi & \cos\phi\cos\psi + \sin\phi\sin\theta\sin\psi & -\sin\phi\cos\psi + \cos\phi\sin\theta\sin\psi \\ -\sin\theta & \sin\phi\cos\theta & \cos\phi\cos\theta \end{vmatrix}$$

(3.6)

Similar to the body-to-navigation frame rotation is the navigation frame to Earth frame rotation. The Earth frame's origin resides at the planet's center and its principle axes are fixed to the Earth and rotate along with it. In this frame, the positive z-axis extends through the North Pole, while the x-axis is aligned with the intersection of the prime meridian and the equator. The y-axis is orthogonal to the aforementioned axes, and obeys the right-hand rule [59]. Equation 3.7, derived in a similar manner to the body frame to navigation frame DCM, is used for the navigation frame to Earth frame rotation.

$$\mathbf{C_n^e} = \begin{vmatrix} -\cos w\sin L\cos\lambda + \sin w\sin\lambda & -\sin w\sin L\cos\lambda - \cos w\sin\lambda & -\cos L\cos\lambda \\ -\cos w\sin L\sin\lambda - \sin w\cos\lambda & -\sin w\sin L\sin\lambda + \cos w\cos\lambda & -\cos L\sin\lambda \\ \cos w\cos L & \sin w\cos L & -\sin L \end{vmatrix}$$

(3.7)

The DCM provided above requires the longitude, L, and latitude, λ, of the aircraft in addition to the angle between north and x-axis of the wander frame, known as the wander angle, w [59]. The concept for wander angle is used to compensate for heading being undefined at the Earth's Pole.

3.3 Linear Interpolation

The sensor data collected onboard Ohio University's DC-3 are collected at different rates for different sensors. As a result, the measurements from remote sensors and navigation sensors are valid at different times. However, since these measurements are properly time tagged with GPS timestamps, interpolation can be used for rate adjustment and synchronization. Linear interpolation is performed between point *a* and point *b* via Equation 3.8

$$y = y_a + (x - x_a)\frac{y_b - y_a}{x_b - x_a} \tag{3.8}$$

where x_a and y_a are the coordinates of point *a*, x_b and y_b are the coordinates of point *b*, and *x* and *y* are the coordinates of the interpolation results.

3.4 3-D Plane Fitting

A three dimensional point cloud is made up of a collection of vertices expressed as an ordered triple in *X*, *Y*, and *Z* coordinates. Sets of points within the cloud may describe the surface of an object or the surfaces of many objects in a single scene. Approximations of flat surfaces can often be computed by fitting a plane through the point cloud, while taking all vertices into consideration. This surface representation is known as a best-fit plane. The method used in this research for terrain modeling and extraction from ALS data, that requires calculation of best-fit planes, is described in Equation 3.9 to Equation 3.16 and is based on the method developed in [60].

One possible equation used to describe a plane is given by Equation 3.9.

$$z = Ax + By + C \tag{3.9}$$

In Equation 3.9, A, B, and C are constants determined by minimizing the sum of the squared errors between each vertices' z-component, z_i, and the planar representation of Equation 3.10.

$$Ax_i + By_i + C \tag{3.10}$$

The sum of squares error function is formulated in Equation 3.11

$$E(A,B,C) = \sum_{i=1}^{m}[(Ax_i + By_i + C) - z_i]^2 \tag{3.11}$$

and can be solved by setting the gradient of the error to zero, as in Equation 3.12.

$$(0,0,0) = \nabla E = 2\sum_{i=1}^{m}[(Ax_i + By_i + C) - z_i](x^i, y_i, 1) \tag{3.12}$$

The solution of Equation 3.12 can be expressed as a system of linear equations, in which the constants A, B, and C are unknown. Equation 3.13 formulates that solution and is equivalent to the least squares solution of the minimization of $E(A,B,C)$. The mathematical process of least squares is described in Section 3.4.

$$
\begin{bmatrix} \sum_{i=1}^{m} x_i^{\,2} & \sum_{i=1}^{m} x_i y_i & \sum_{i=1}^{m} x_i \\ \sum_{i=1}^{m} x_i y_i & \sum_{i=1}^{m} y_i^{\,2} & \sum_{i=1}^{m} y_i \\ \sum_{i=1}^{m} x_i & \sum_{i=1}^{m} y_i & \sum_{i=1}^{m} 1 \end{bmatrix} \cdot \begin{bmatrix} A \\ B \\ C \end{bmatrix} = \begin{bmatrix} \sum_{i=1}^{m} x_i z_i \\ \sum_{i=1}^{m} y_i z_i \\ \sum_{i=1}^{m} z_i \end{bmatrix} \tag{3.13}
$$

3.5 Weighted Least Squares Algorithm

The method of weighted least squares is used to optimize the fitting of a model to a set of data. In the case of this research, a weighted least squares approach is used to optimize the best-fit plane detailed in Section 3.3, which is used to distinguish LIDAR points belong to terrain from points belonging to features. The least squares regression method along with the following equations is described in [61][62]. The basic formulation of a least squares problem is given as,

$$
\mathbf{Y} = \mathbf{HX} \tag{3.14}
$$

and can be solved in the weighted sense using

$$
\mathbf{WY} = \mathbf{WHX} \tag{3.15}
$$

to obtain the following solution for *X*, as in Equation 3.16.

$$\mathbf{X} = (\mathbf{H^T WH})^{-1}(\mathbf{H^T WY}) \qquad\qquad (3.16)$$

The weight matrix used in Equation 3.15 and Equation 3.16 is a diagonal matrix composed of weights corresponding to each measurement in the *Y* vector and *H* matrix.

3.6 K-means Clustering

In this research, recognition of features within ALS data is accomplished via clustering, using an unsupervised pattern recognition method. Clustering techniques are used to group individual items of a set into smaller subsets based on specific measures of either similarity or dissimilarity. In the case of 3-D point clouds, an appropriate metric used to determine dissimilarity is the point-to-point Euclidean distance. The *k*-means algorithm, described in this section and [63], is used as the clustering technique for recognizing features, specifically ground vehicles, in this research.

The *k*-means algorithm first chooses *n* cluster center estimates, where *n* is a predetermined number of clusters. These centers are often chosen randomly, however, the algorithm's performance improves as the accuracy of the initial center estimation increases [64]. Once the cluster centers have been estimated, the dissimilarity metric is applied to assign all non-center points to a specific cluster. After this has been accomplished the process undergoes another iteration, this time choosing a cluster center based on the resultant cluster from the previous iteration. This algorithm continues until convergence is reached when cluster centers no longer change location specifically

during consecutive iterations. The outcome of this process yields well-defined clusters representing features within the point cloud. One major disadvantage of this method is that the number of clusters must be known *a priori*.
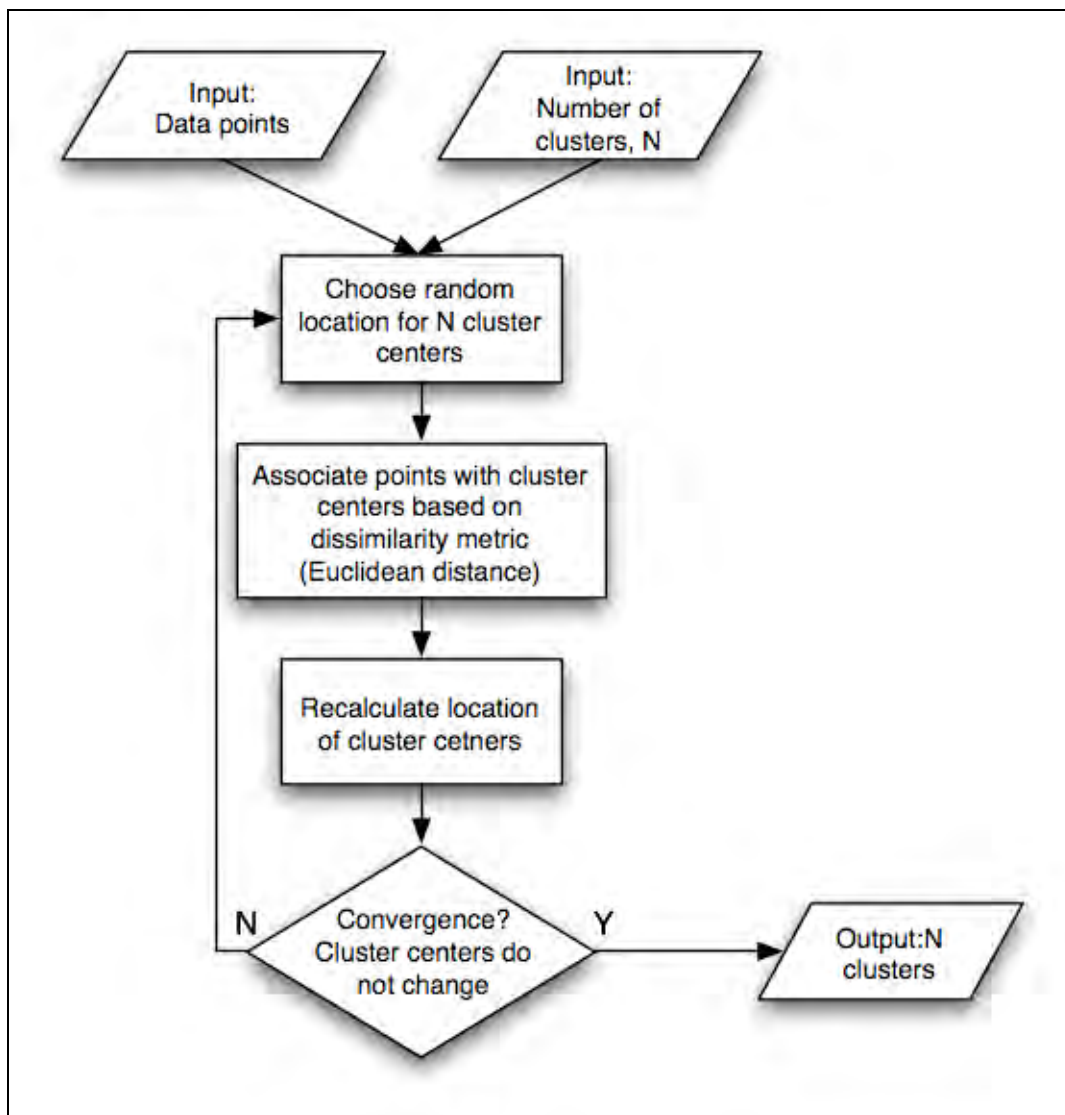
Figure 3.2: k-means clustering flowchart

CHAPTER 4: METHODOLOGY

4.1 Concept

The goal of this research is to detect mobile obstacles, such as a vehicle, that may prove

to be a safety hazard during approach and landing procedures. This is accomplished using

two ALS sensors along with inertial and GPS navigation information. Each ALS scans

the runway and then uses the processing techniques described in this chapter to search for

any measurement that likely does not belong to terrain and can be considered a scene

feature. These scene feature measurements are then grouped into sets of 3D points each

composing a potential hazard. Since two ALS sensors are used each hazard is detected at

two different times and locations. The dual detection can be used to form a linear velocity

estimate of the hazard.

4.2 Experiment Overview

LIDAR data of an obstacle in motion along a runway was collected via flight tests

performed at the Ohio University Airport (KUNI) in Albany, Ohio. Ohio University's

1943 Douglas DC-3 Flying Laboratory experimental aircraft is equipped with GPS, a

navigation grade Inertial Reference Unit (IRU), a CCD camera, and two airborne laser

scanners. This sensor suite was used to scan the runway for hazards while flying an

aircraft approach for landing. A conversion van approximately 2 m in height and 5.5

meters in length was driven on the runway during aircraft fly-over, serving as a mobile

runway hazard. The van was equipped with a GPS receiver in order to verify the precise

location of the vehicle during the experiment. In this experiment, the ALSs were mounted

in a downward looking manner resulting in hazard detection and state estimation when

the aircraft is located directly over the hazard. For an actual hazard detection system both

ALSs must be pointed forward so hazards can be anticipated before they become a safety

risk.

4.3 Vehicle Hazard

The mobile hazard used in flight experimentation was a conversion van capable of

housing data collection equipment. Mounted on top of the van, approximately 0.5 meters

above the roof was a NovAtel pinwheel GPS antenna. This antenna was used in

conjunction with a NovAtel OEM4 GPS receiver. Logging of the navigation data from

the receiver was performed with GPS Data Logger 3.17, a software package from

Waypoint Consulting. An image of the van hazard is provided in Figure 4.1.

Figure 4.1: The mobile hazard used for data collection

4.4 System Configuration

Resolving the precise location of the ALS footprints requires the aircraft's navigation

solution. A NovAtel OEM4 L1/L2/WAAS GPS receiver and a Honeywell HG1150 IRU

were used to capture and subsequently process the aircraft position and attitude

information. The GPS receiver also functioned as a time reference used to time-tag all

measurements made by the hazard monitor's instruments and sensors with the GPS week

number and time of week. Section 4.4.1 and Section 4.4.2 provide detailed technical

specifications of the IMU and GPS receiver, respectively. Each of the devices described

above rely on the navigation computer for reading, time tagging, and storing data in an

utilizable format.

LIDAR measurements were performed with Riegl's LMS-Q140i Airborne Laser Scanner

and LMS-Q280i Airborne Laser Scanner. These sensors capture time-of-flight

data, which are then converted into range measurements, along with the corresponding

scan angles from the laser's linear scanning pattern. Recording of ALS data was

accomplished with a data collection computer, communicating with the laser scanners via

Ethernet and parallel port interfaces. During the capture of each laser point, the data

collection computer, using the precision timing measurements output by the GPS

receiver, performed time tagging. Further technical details on each ALS are provided in

Section 4.4.3. In addition to laser information, the data collection computer was

responsible for the storage and time tagging of still images captured by the Prosilica

GC1350C CCD (Charge Coupled Device) camera, described in further detail in Section

4.4.4. The images were encoded in an 8-bit Bayer pattern and later decoded into an RGB

image during post-processing. An overview of the instruments, sensors, and their

measurements used in the hazard monitoring system is provided in Figure 4.2.
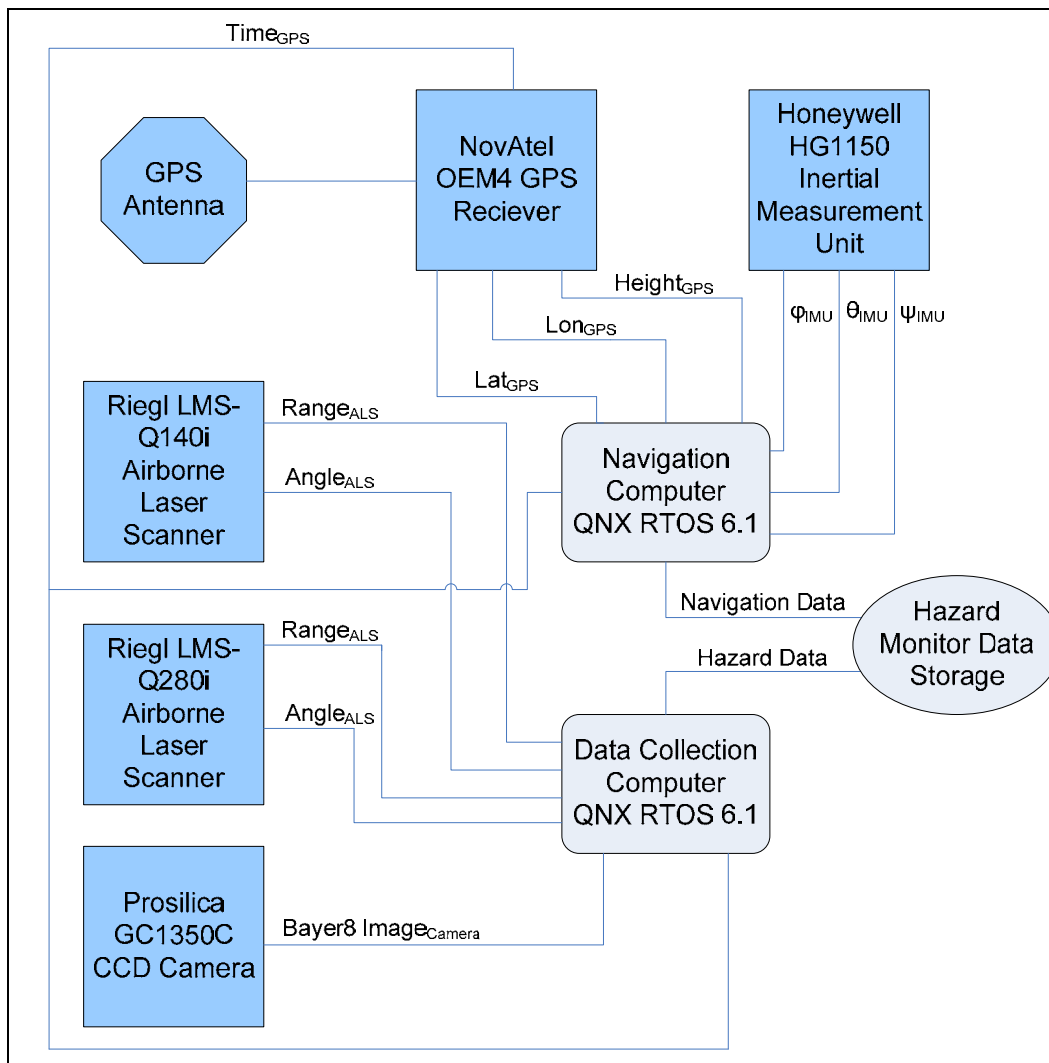
Figure 4.2: System components diagram

4.5 System Components

4.5.1 Inertial Measurement Unit

Aircraft attitude measurements were obtained with a Honeywell HG1150 IRU. This rack-mounted device consists of Ring Laser Gyros (RLG) and accelerometers capable of providing attitude, velocity, and position data. Attitude information from the HG1150

was used to compensate ALS measurements for the orientation of the aircraft when geo-referencing the laser footprints. Technical specification of the Honeywell HG1150 IRU are provided in Table 4.1

Table 4.1

IMU Technical Specifications [65]

Inertial Measurement Unit	
Specification	**Value**
Model	Honeywell HG1150DB02 Navigation Grade Inertial Reference Unit
Type	Ring Laser Gyro (RLG)
Position Drift	1 nmi / hour
Data Rates	Horizontal Velocity – 20 Hz Vertical Velocity – 25 Hz Pitch – 50 Hz Roll – 50 Hz Heading – 20 Hz
Data Bandwidth	Horizontal Velocity – 2 Hz Vertical Velocity – 8 Hz Pitch – 8 Hz Roll – 8 Hz Heading – 2 Hz
Interface	ARINC-29

4.5.2 GPS Receiver

The external hazard monitor uses a NovAtel OEM4 L1/L2/WAAS GPS receiver to provide aircraft positioning information and perform the precision time keeping functionality necessary for time synchronization of measurements from other onboard sensors. NovAtel's OEM4 receiver is capable of outputting position rates at up to 20 Hz with a circular error probable of 0.8 m when making use of the L1, L2, and WAAS

channels [66]. A kinematic differential positioning solution is obtained via post

processing of the data using GrafNav, a software package available from Waypoint

Products Group. Table 4.2 details the technical specifications of this unit.

Table 4.2

Onboard GPS Technical Specifications [66]

Onboard GPS	
Specification	**Value**
Model	NovAtel OEM4
Channels	L1 L2 WAAS
Measurement Rate	20 Hz
Position Rate	20 Hz
Time Accuracy	20 ns RMS
Circular Error Probable (CEP)	L1 – 1.8 m L1/L2 – 1.5 m L1/WAAS – 1.2 m L1/L2/WAAS – 0.8 m
Interface	Serial RS-232

4.5.3 Airborne Laser Scanners

The dual ALS system is made up of a Riegl LMS-Q140i Airborne Laser Scanner and a

Riegl LMS-Q280i Airborne Laser Scanner. Both 2D scanners perform terrain

measurements via pulsed laser at a wavelength of 0.9 μm. The gating mechanism is

controlled by a rotating polygon mirror and is located inside the ALS housing [67][68].

The rotation of the multifaceted mirrors allow angle and range measurements to be

acquired in a raster pattern. Two-dimensional laser data obtains a third dimension when the laser in put into motion during scanning.

There is a significant difference in the maximum range, accuracy, and angular resolution between the two laser scanners. High costs associated with such instruments has lead to limitations of the breath of testing performed with the lasers, however, experimentation in this research has been specifically designed to compensate for many differences. Detailed technical specifications of both ALSs are displayed in Table 4.3. In this table, the variable ρ represents the reflectance of the imaged surface.

Table 4.3

ALS Technical Specifications [67][68]

Airborne Laser Scanners		
Specification	**Riegl LMS-Q280i ALS**	**Riegl LMS-Q140i ALS**
Scanning Mechanism	Rotating Polygon Mirror	Rotating Polygon Mirror
Number of Mirror Facets	4	3
Maximum Range	850 m for $\rho \geq 20\%$ 1500 m for $\rho \geq 80\%$ 2000 m maximum	150 m for $\rho \geq 10\%$ 450 m for $\rho \geq 80\%$ 700 m maximum
Minimum Range	30 m	2 m
Measurement Accuracy	±20 mm	±5 cm
Wavelength	1 μm Near Infrared	0.9 μm Near Infrared
Pulse Repetition Rate	24 kHz	30 kHz
Scan Angle	45° at 100% Range or 60° at 90% Range	80°
Angular Resolution	0.0025°	0.036°
Laser Beam Divergence	0.5 mrad	3.0 mrad
Interface	Serial RS-232 Parallel ECP Ethernet TCP/IP	Parallel ECP
Eye Safety	Class 1 (Eye Safe)	Class 1 (Eye Safe)

4.5.4 Camera

A downward-looking Prosilica GC1350C CCD camera was used to capture terrain

images containing potential runway hazards in the visible light spectrum of 400 nm to

1000nm. Using 8-bit Bayer encoding, the camera was able to achieve an image resolution

of 1360-by-1024 pixels [69]. Further post processing of the Bayer pattern data was

performed to obtain an RGB image. Table 4.4 provides detailed specifications of the

camera. CCD exposure time was automatically adjusted by the camera based on the

amount of light in the scene. The program driver, responsible for operating the camera and storing images used software based triggering for image acquisition. Once the previous image was written to memory in the data collection computer the next image was captured. Due to the processing load on the data collection computer, the software-triggered camera was only able to achieve frame rates in the range of 2 Hz to 7 Hz. An image displaying the installation of the GC1350C camera in the fuselage's hazard monitor bay of the aircraft is provided in Figure 4.3.

Table 4.4

Camera Technical Specifications [69]

CCD Camera	
Specification	**Value**
Model	Prosilica GC1350C
Sensor	Sony ICX205 ½" CCD, Super HAD Progressive Scan
Resolution	1360x1024
Spectral Range	400 nm – 1000nm
Maximum Frame Rate	20 FPS
Exposure Range	20 μsec – 60 μsec
Gain	0 dB – 22 dB
Imaging Modes	External Trigger Fixed Frame Rate Software Trigger
Color Modes	Bayer8, Bayer16, RGB24, BGR24, RGBA24, BGRA24, YUV411, YUV422, YUV444
Interface	802.3 IEEE 1000baseT Ethernet
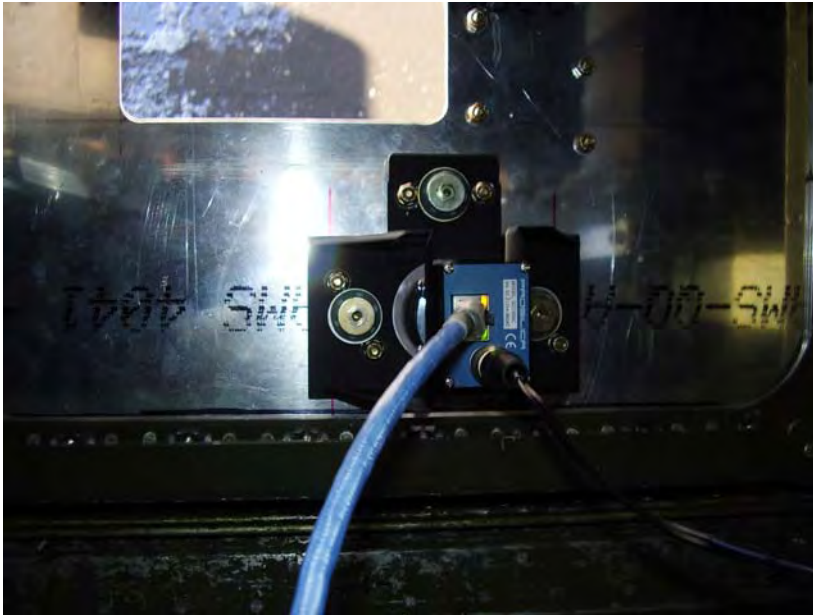
Figure 4.3: GC1350C CCD camera installation

Like all other components of the hazard monitor, camera data was time tagged with GPS

time of week information immediately proceeding acquisition. Time-tagged camera data

is used in this experiment to assist with manually parsing flight data relevant to the

experiment, although with further uses and integration techniques are discussed in

Section 6.3.

4.6 Experimental Procedure

With the configuration of the two laser scanners onboard the DC-3, it is possible to sense

a runway hazard at time, t, by ALS_1, and again at time $t+1$, by ALS_2. The optimal

location of these sensors on the aircraft is in the nose of the plane, with both ALS_1 and

ALS_2 looking forward at separate pointing angles. Since this particular configuration was

not available at the time of the experiment and is cost prohibitive at the current time, the

laser scanner configuration used for terrain navigation was used to evaluate the concepts

described in this thesis. The LMS-Q140i ALS was mounted as a downward-looking

sensor at an angle of 0° from the Z-axis of the aircraft body frame. The longer range

LMS-Q280i was mounted at a forward-looking angle of 30.5° from the aircraft body

frame's Z-axis. The laser installation and hazard monitor bay are shown in Figure 4.4
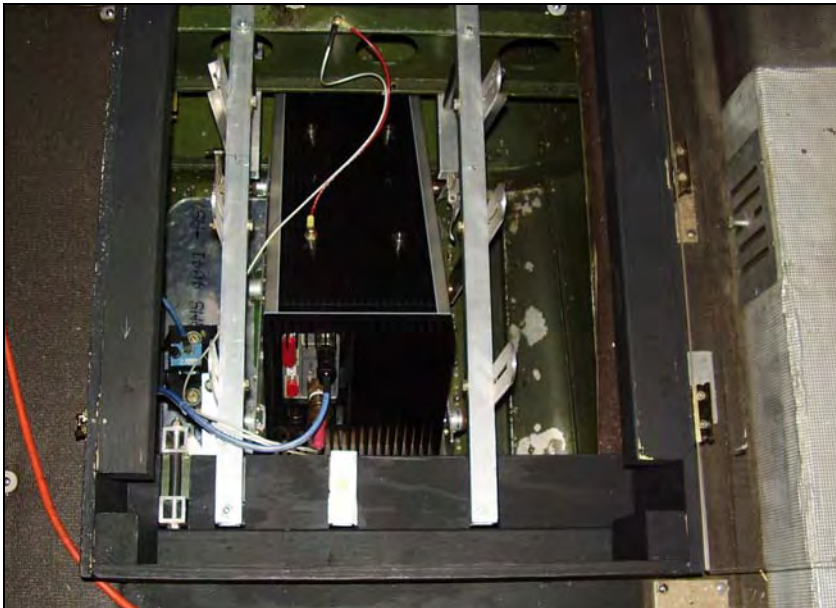
Figure 4.4: The hazard monitor bay including the dual ALS installation

Selection of proper laser scanner parameters is integral to the hazard monitor's ability to

detect specific hazards. When measuring hazards as small as a van or other similar

ground vehicles, a high laser point density is necessary, while a large field of view is less

important. Both laser scanners were set to perform measurements at a rate of 30 scan

lines per second at a pulse repetition rate of 24 kHz. The field of view of the LMS-Q280i

was set at 45°, while the LMS-Q140i was set at 60°.

ALS data were collected on three similar aircraft fly-overs, with the motion of the mobile

van hazard varying on each approach. During fly-over experiment number one, the van

was driving along the centerline of the runway, moving in the same direction as the

aircraft, while being scanned by the onboard lasers of the overhead aircraft. The second

experiment was performed similar to the first, however, in this scenario, the van was

driving along the centerline of the runway in the opposite direction of the aircraft motion.

Finally, in experiment 3, the van is moving in a zigzag pattern across the runway. Figure

4.5 details the position of the van during each trial, while Figure 4.6 and Figure 4.7 are

plots of the aircraft's flight path during data collection.
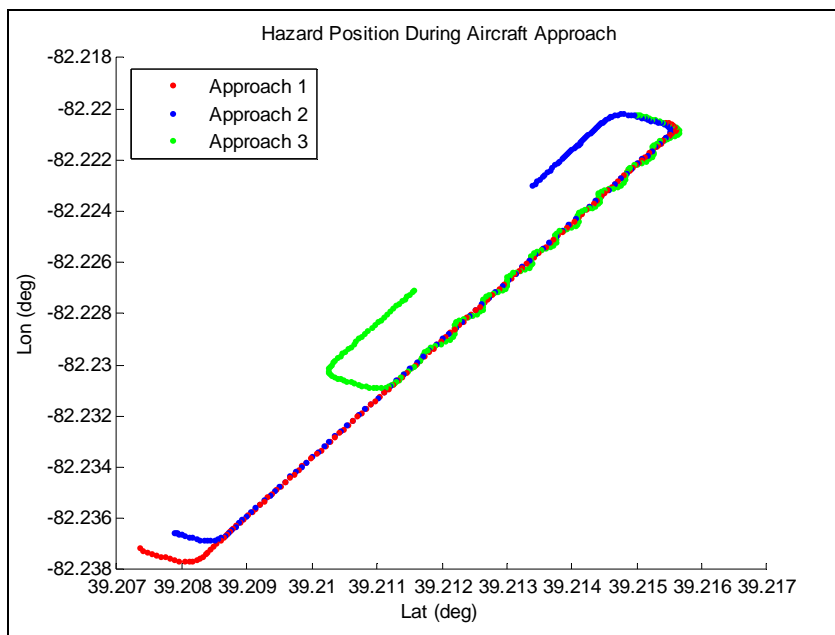
Figure 4.5: Van position during all three fly-overs
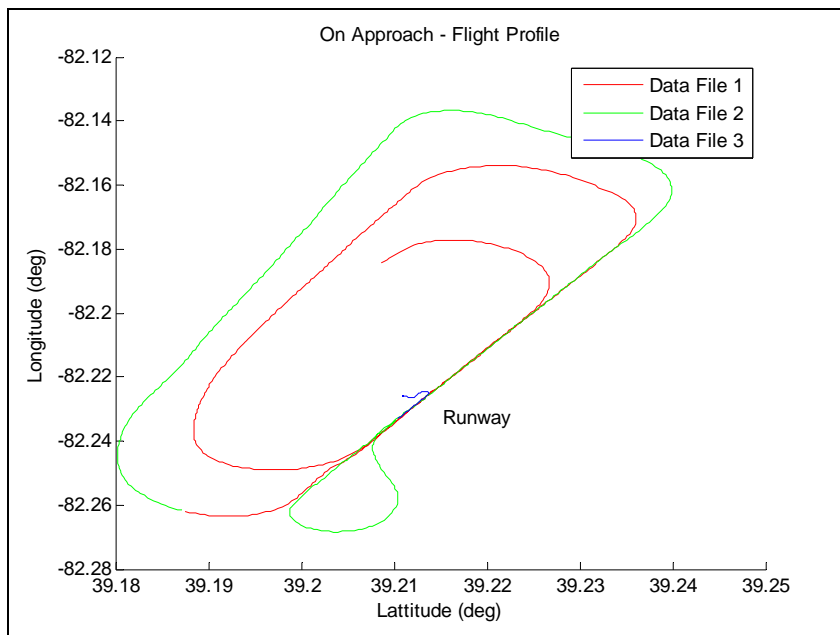
Figure 4.6: Aircraft flight profile – latitude and longitude
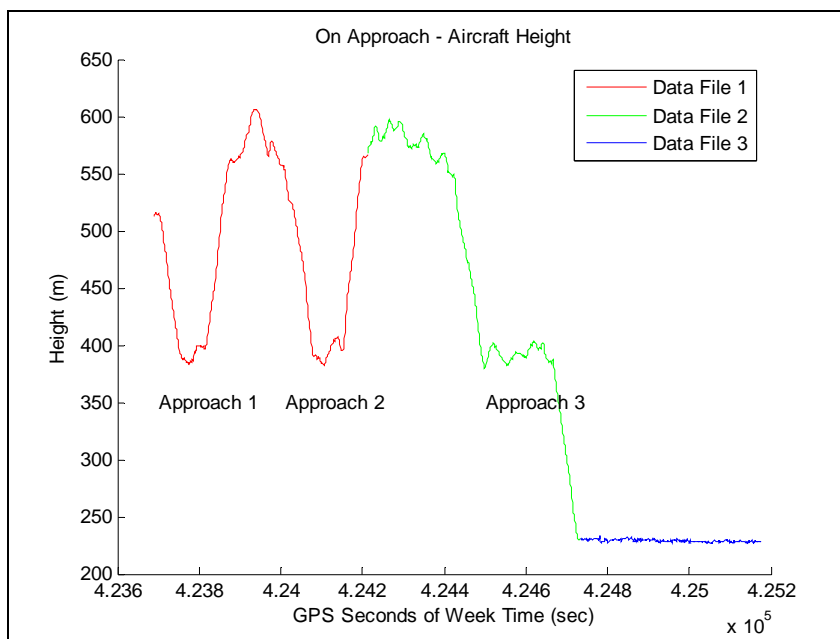
Figure 4.7: Aircraft flight profile – height

4.7 Geo-referencing of Laser Footprints

Upon collection of all navigation and sensor measurements, the following procedure is used to detect, geo-reference, and estimate the state of runway hazards. Geo-referencing of the ALS footprints is defined as the estimation of the precise location of all laser scan points in a rotating frame fixed to the Earth. In order to accomplish this task, the position and orientation of the measurement platform, the aircraft in this case, must be known in addition to any lever-arm or orientation offsets caused by placing the sensors at different locations and mounting angles. Not all data from the flight test were collected at the same frequency so it must be synchronized, providing a GPS position, an IMU orientation, and a time measurement for each laser footprint. To accomplish synchronization, interpolation of position and orientation angles at each measurement point was performed using the linear interpolation method described in Section 3.2. The geo-referencing of the now synchronized data is accomplished in a manner similar to that discussed in [7].

The first step in the geo-referencing process involves expressing the LIDAR range and angle measurements in a reference frame relative to the orientation of the ALS. A DCM is used in the following equation to perform a single coordinate rotation from the laser measurement frame, X_{LM}, to the laser body frame, X_{ALS}

$$\mathbf{x_{Laser}} = \mathbf{C_{LM}^{Laser}}(\mathbf{f_i}, \mathbf{q_i}, \mathbf{y_i}) \cdot \begin{vmatrix} 0 \\ 0 \\ r_i \end{vmatrix} \tag{4.1}$$

where r_i is the range from the ALS to the ground as measured by the laser and

$\mathbf{C_{LM}^{Laser}(f_i,q_i,y_i)}$ is the DCM used to convert from $\mathbf{x_{LM}}$ to $\mathbf{x_{Laser}}$. In this scenario the

mounting angle of the laser can be expressed as the pitch, θ_L. The pitch in the case of the

downward looking LMS-Q140i is 0°. The LMS-Q280i is pointed at a forward angle of

30.5° from the vertical axis, resulting in a 30.5° pitch. The scanning angle of the laser

can be expressed as roll, φ_L, about the bore-sight axis of the laser. No information is

required to represent the difference in heading, ψ_L, since the laser measurement data and

the laser frame are aligned. Equation 4.2 is a representation of the DCM, $\mathbf{C_{LM}^{Laser}(f_i,q_i,y_i)}$

$$\mathbf{C_{LM}^{Laser}} = \begin{vmatrix} \cos\theta_L \cos\psi_L & -\cos\theta\sin\psi + \sin\phi_L \sin\theta_L \cos\psi_L & \sin\phi_L \sin\psi_L + \cos\phi_L \sin\theta_L \cos\psi_L \\ \cos\theta_L \sin\psi_L & \cos\theta_L \cos\psi_L + \sin\phi_L \sin\theta_L \sin\psi_L & -\sin\phi_L \sin\psi_L + \cos\phi_L \sin\theta_L \sin\psi_L \\ -\sin\theta_L & \sin\phi_L \cos\theta_L & \cos\phi_L \cos\theta_L \end{vmatrix}$$

$$(4.2)$$

Once the measurement frame's heading alignment with the ALS has been taken into

account the DCM of Equation 4.2 simplifies into Equation 4.3.

$$\mathbf{C_{LM}^{Laser}} = \begin{vmatrix} \cos\phi_L \sin\theta_L \\ \sin\phi_L \\ \cos\phi_L \cos\theta_L \end{vmatrix} \qquad (4.3)$$

The rotation into the ALS body frame, $\mathbf{X_{ALS}}$, from Equation 4.1 can now simply be

expressed as

$$\mathbf{x}_{\mathbf{LM}}^{\mathbf{Laser}} = \begin{vmatrix} \cos\phi_L \sin\theta_L & 0 \\ \sin\phi_L & 0 \\ \cos\phi_L \cos\theta_L & r_i \end{vmatrix} \tag{4.4}$$

The next step in the geo-referencing process requires a conversion from the laser body

frame, X_{ALS}, to the aircraft body frame, X_B. This is performed with a DCM similar to

Equation 4.2 to compensate for the misorientation created by the mounting angles of the

IMU. It must also take into account the lever arm offset created by the placement of the

craft's GPS antenna. The lever arm measured from the GPS antenna to the ALS inside

the aircraft was measured using the centerline of the aircraft as a reference point. The

IMU misorientation was not measured, however, it is assumed to be small, at an angle of

less than 2° along each axis. For this research, zero misorientation was assumed since

measurement proved difficult due to lack of measuring devices. Equation 4.5 now

becomes simplified, since no rotation is required. Taking the preceding instrument and

sensor location and orientation into account the conversion to the aircraft body frame is

completed using the following

$$\mathbf{X_B} = \mathbf{L_{GPS \to ALS}} + \mathbf{X_{ALS}} \tag{4.5}$$

All ALS footprints are now expressed in the body frame of the aircraft. The next step

requires a rotation to the navigation frame, where the axes are aligned with the north,

east, and down directions. Equation 4.6 represents this rotation and makes use of the

DCM of Equation 4.7 that is proposed in Section 3.6.

$$\mathbf{X_N} = \mathbf{C_B^N X_B} \tag{4.6}$$

where

$$\mathbf{C_B^N} = \begin{vmatrix} \cos\theta\cos\psi & -\cos\theta\sin\psi + \sin\phi\sin\theta\cos\psi & \sin\phi\sin\psi + \cos\phi\sin\theta\cos\psi \\ \cos\theta\sin\psi & \cos\phi\cos\psi + \sin\phi\sin\theta\sin\psi & -\sin\phi\cos\psi + \cos\phi\sin\theta\sin\psi \\ -\sin\theta & \sin\phi\cos\theta & \cos\phi\cos\theta \end{vmatrix} \tag{4.7}$$

The final step of the geo-referencing process is conversion into the Earth frame. This requires the aircraft position, X_{Craft}, plus a DCM making use of the craft latitude, L, the longitude, λ, and the wander angle, w. This translation and rotation is shown in Equation 4.8 and 4.9

$$\mathbf{X_E} = \mathbf{X_{Craft}} + \mathbf{C_N^E X_N} \tag{4.8}$$

where

$$\mathbf{C_n^e} = \begin{vmatrix} -\cos w\sin L\cos\lambda + \sin w\sin\lambda & -\sin w\sin L\cos\lambda - \cos w\sin\lambda & -\cos L\cos\lambda \\ -\cos w\sin L\sin\lambda - \sin w\cos\lambda & -\sin w\sin L\sin\lambda + \cos w\cos\lambda & -\cos L\sin\lambda \\ \cos w\cos L & \sin w\cos L & -\sin L \end{vmatrix} \tag{4.9}$$

An overview of the geo-referencing method used in this thesis is given in Figure 4.8.
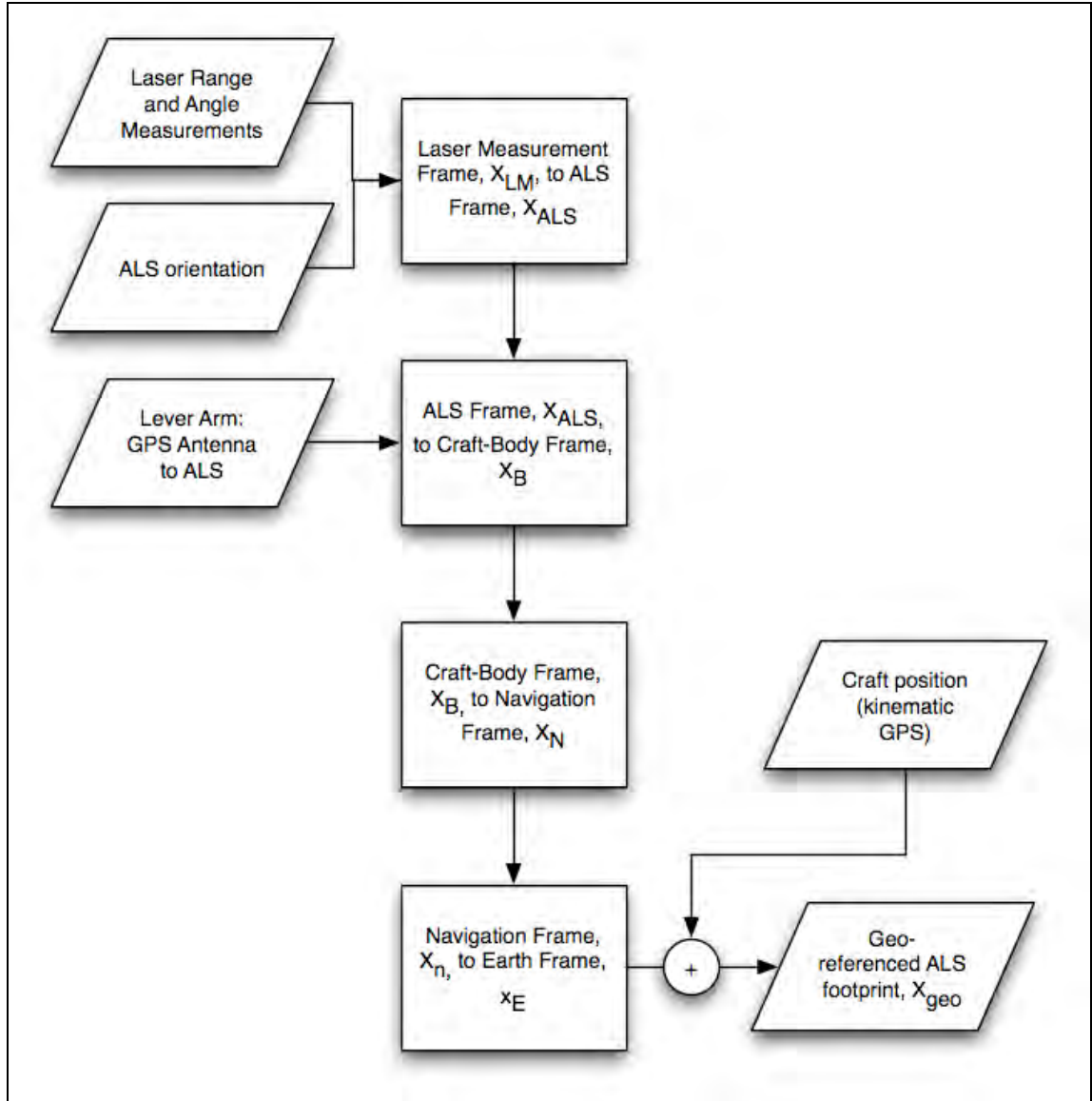
Figure 4.8: Geo-referencing of ALS footprints flow chart

4.8 Windowed Weighted Least Squares Terrain Estimation

After all laser footprints have been geo-referenced, the next step in the process is to

separate measurements belonging to the terrain and measurements that are considered to

be features of the scene. Any identified scene feature LIDAR footprint will initially be

considered a hazard. Since the hazard detection used in this research is intended for runway landings, it is possible to take advantage of the flat surface geometry of runways and taxiways. This allows for laser footprints residing above an empirically determined surface estimate to be considered part of a scene feature and thus a hazard. The method discussed in this section is derived from the method used in [8] and [70].

The feature separation algorithm begins by converting all geo-referenced measurements from an ECEF system into a local-level coordinate system, expressed in North-East-Down (NED) coordinates. This allows for more intuitive representation of the scene and has the added benefit of defining laser points with respect to a reference point, in this case a point located on the runway. Next, all erroneous ALS measurements are filtered out of the data. These erroneous data points likely originate from measurement errors within the ALS and appear as points residing at an unrealistic location above a threshold of 100 m from the runway surface. Further filtering of the data then occurs to eliminate measurements located too far away, in a lateral sense, from the runway surface area. The distance of these points from the region of interest, the runway, makes them unnecessary in monitoring scenarios and has the disadvantage of increased computation time and poorer algorithm performance by possibly including terrain with steep gradients. Elimination is performed by truncating the ALS measurements to only include a laser sweep angle of 5° from nadir in both directions. This angle takes into account the altitude of the aircraft and the width of the runway and would be required to expand if the craft's altitude decreases.

Now that all unnecessary data has been eliminated, the measurements are broken up into small regions, or windows, each representing 0.5 sec of data. Windowing of data allows the weighted least squares terrain estimation algorithm to operate over a small region, likely consisting of a single smooth surface. Non-linear variations in the terrain such as gradients and hills should not occur in such a small window, thus increasing algorithm performance. The choice of 0.5 sec as the window size was determined experimentally and appears to yield acceptable results.

Each 3-D point cloud window is now operated on individually. First a best-fit plane is constructed through the ALS point cloud window, as described in Section 3.3 to solve for the coefficients of Equation 4.10.

$$z = Ax + By + C \tag{4.10}$$

Now that the best-fit plane has been obtained, the next step in the algorithm is to decide whether ALS points belong to terrain or to features. This is done by assigning weights to points based on an estimate as to whether they belong in the set of terrain points or feature points. The point weights are continuously reassigned as the windowed weighted least squares algorithm iterates before converging on a solution. In the solution, all points have been assigned a weight of zero (terrain) or one (feature). Eventually all non-terrain points will be removed from the data, as they are assigned a weight of zero.

In order to determine the point weights, the height residuals between the actual ALS measurements and the points of the best-fit plane first need to be calculated. Equation 4.11 describes this process.

$$R_i = \left| z_p - z_i \right|$$ (4.11)

The height residual values were then put into a histogram. The bins of the histogram are made up of a small range of the height residual from Equation 4.11. The bin of the largest magnitude, containing the most values in its residual range, is selected to provide information to the weighting function, which is used to assign the point weights mentioned above. The center value of the histogram's largest bin was selected as the weighting parameter, g. The definition of this weight function given in [70] is expressed in Equation 4.12.

$$w_i = \begin{cases} 1 & R_i < g \\ \dfrac{1}{1 + \alpha(R_i - g)^{\beta}} & g < R_i < g + M \\ 0 & g + M < R_i \end{cases}$$ (4.12)

In the above equation w_i is the weight of the ALS measurement, g is the weighting parameter, and σ_{Ri} is the value of the largest bin of the height residual histogram. M, α, and β are constants that were determined experimentally in [70] where

M= 0.9

α=1

β=4

A visualization of this weighting function can be found in Figure 4.9. In essence, this method is based on the fact that a majority of the scanned points belong to the terrain and will have a smaller residual value since they are closer to the planar surface. Points above the planar surface (i.e. belonging to a feature) will have larger residual values and will be assigned a smaller weight during the next iteration of the planar fit.
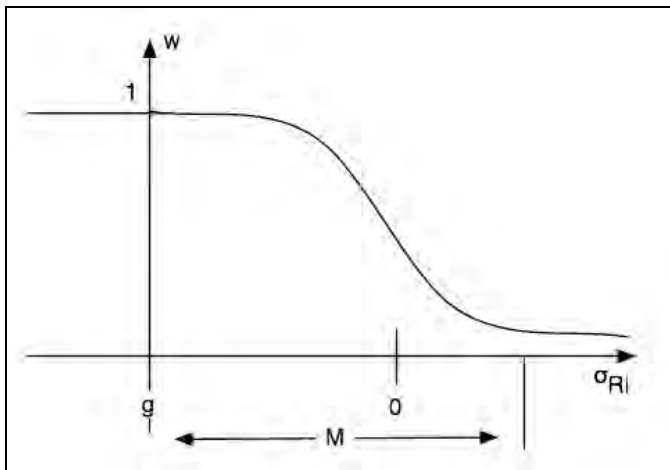
Figure 4.9: Weight function used to determine terrain points from non-terrain [70]

Once Equation 4.12 has been used to assign new weights to all ALS points, these weight values are fed into the best-fit plane calculation to determine a new best-weighted least squares fit plane following Equation 4.13

$$\begin{bmatrix} \sum_{i=1}^{m} x_i^2 w_i & \sum_{i=1}^{m} x_i y_i w_i & \sum_{i=1}^{m} x_i w_i \\ \sum_{i=1}^{m} x_i y_i w_i & \sum_{i=1}^{m} y_i^2 w_i & \sum_{i=1}^{m} y_i w_i \\ \sum_{i=1}^{m} x_i w_i & \sum_{i=1}^{m} y_i w_i & \sum_{i=1}^{m} w_i \end{bmatrix} \cdot \begin{bmatrix} A \\ B \\ C \end{bmatrix} = \begin{bmatrix} \sum_{i=1}^{m} x_i z_i w_i \\ \sum_{i=1}^{m} y_i z_i w_i \\ \sum_{i=1}^{m} z_i w_i \end{bmatrix} \tag{4.13}$$

The height residuals are then recalculated and the weighting process is repeated. This process continues until all points have been classified with a weight of zero or one and the algorithm converges. All windows of ALS measurements undergo this same process resulting in two sets of points, one consisting of terrain and the other consisting of non-terrain features. An overview of this method is given below in Figure 4.10.
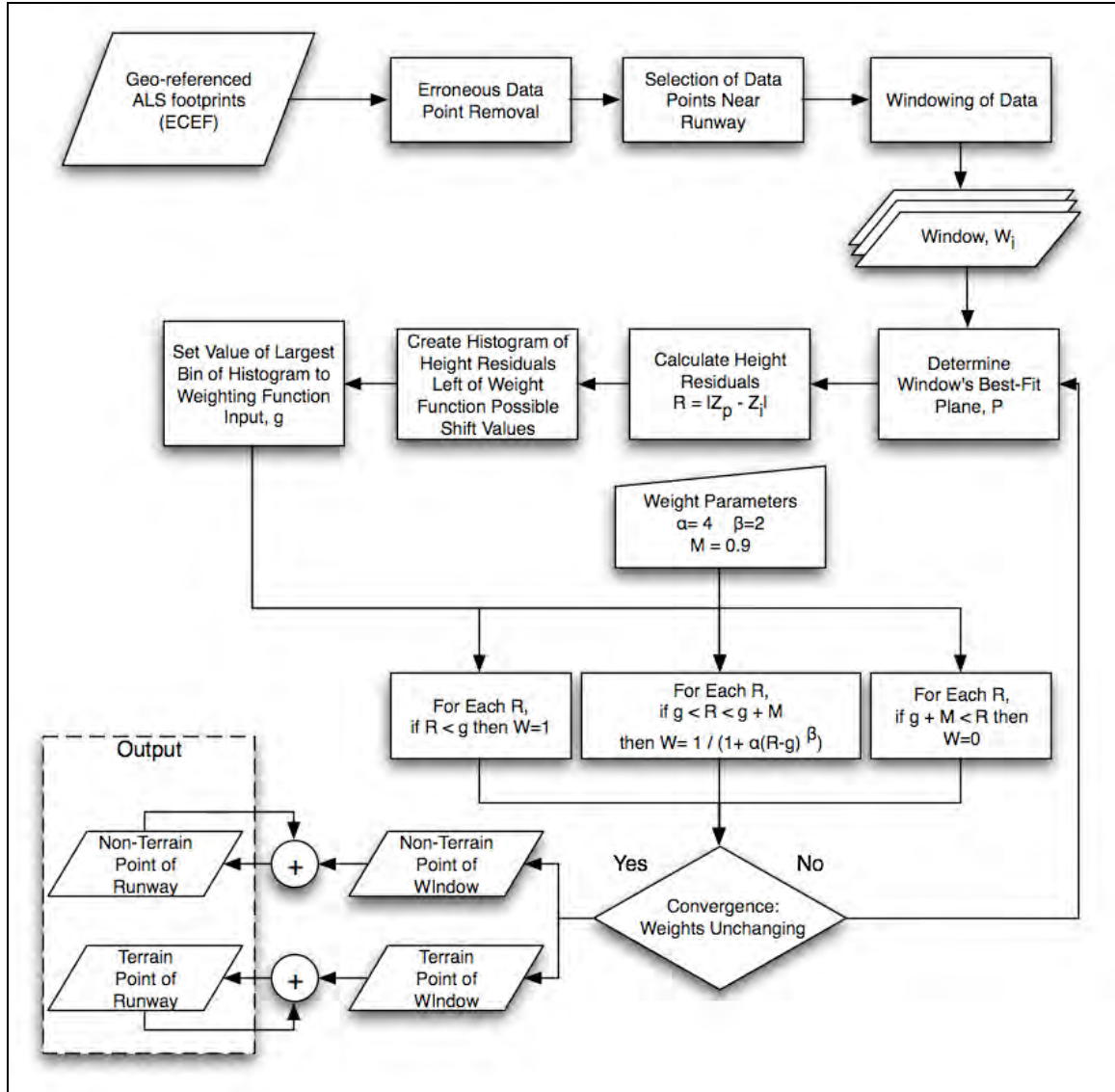
Figure 4.10: ALS point classification flow chart

4.9 Hazard Candidate Clustering

All points have now been classified into sets designating either terrain or scene features, but, with this information it is not possible to assess which points belong to which features. To resolve this problem, the *k*-means clustering algorithm is applied to the

points now residing in the feature set. This method automatically assigns a cluster or
grouping index to all points based on a specific metric and indicates the center location of
each cluster. The metric used in this thesis is a measure of dissimilarity based on the
Euclidian distance from the centroid, $[x_c, y_c, z_c]$ as given in Equation 4.14.

$$d = \sqrt{(x_i - x_c)^2 + (y_i - y_c)^2 + (z_i - z_c)^2}$$
Equation 4.14

Since this method is unsupervised, it assumes that *a priori* knowledge of the data exists,
in this case the number of clusters appearing in the scene, which was determined
experimentally via visual inspection of the data. While this may be seen as a weakness of
k-means clustering, modifications of k-means clustering may be considered that evaluate
the clustering results for a finite set of possible values of '*k*'. However, that investigation
is outside the scope of this thesis.

4.10 Hazard State Estimation

State estimation of a hazard entails approximating the hazard cluster's linear velocity
vector. This is accomplished using data from both ALSs that will likely contain the same
mobile hazard seen at two different times and two different locations. To accomplish this,
the centroid of the vehicle clusters, C_f and C_d from the forward-looking ALS and the
downward-looking ALS are both extracted from the *k*-means clustering results. Using the
time tag information from each data point, provided by GPS, the time of the cluster
measurement is determined. The time of occurrence of the point residing closest to the

center is selected as the hazard time, t_F or t_D, depending on which laser is sensing the hazard. A velocity estimate is now obtained using this information. With only two scene frames available, it is not possible to create an accurate velocity estimate if the hazard is not moving in a linear manner, however, if the hazard is stationary or moving linearly then the simple method of Equation 4.15 can be used to resolve velocity, v_h.

$$v_h = \frac{\sqrt{(X_F - X_D) + (Y_F - Y_D) + (Z_F - Z_D)}}{|t_F - t_D|} \qquad \text{Equation 4.15}$$

In the above equation, X_F, Y_F, and Z_F are the coordinates of the hazard as seen by the forward-looking laser, and X_D, Y_D, and Z_D are hazard coordinates from the downward-looking laser. Note that the use of flash LIDAR sensor could help to achieve a better observability of the velocity since no time uncertainty does exist and the target will be observable in multiple frames.

The result of the algorithm described in Section 4.6 though Section 4.9 yields accurately geo-referenced scene maps capable of identifying potential landing safety hazards and estimating the linear velocity of those hazards.

CHAPTER 5: RESULTS

5.1 Footprint Geo-referencing

Geo-referencing of laser measurements has yielded promising results that appear

accurate. Determining a metric to assess geo-referencing accuracy is difficult, since there

is no way to guarantee that the ALS beam will strike the exact location of the surveyed

point. The method used in this thesis to determine accuracy makes use of the van position

truth information provided by post-processed kinematic DGPS. This reference point can

then be compared temporally and spatially to the ALS measurement point residing closest

in time and location. Various error sources can be attributed to this method including

errors in the kinematic DGPS truth data and the position and time offset of the

measurement point located closest to the reference point. It should be noted that in a real-

time solution to the hazard-monitoring problem kinematic DGPS would not be available,

and would be replaced with either GPS or WASS. An error is introduced by the vertical

lever arm between the roof of the van and the GPS antenna, since it is mounted

approximately 0.5 m above the van. Geo-referencing accuracy can only be assessed

within the performance specified in Equation 5.1

$$E_A = \sqrt{(E_{DGPS_X})^2 + (E_{DGPS_Y})^2 + (E_{DGPS_z})^2 + Z_A^2 + (E_{T_X})^2 + (E_{Ty})^2 + (E_{Tz})^2} \qquad \text{Equation 5.1}$$

where E_{DGPS} is the error due to kinematic differential GPS performance, Z_A is the vertical

lever arm between the van and the antenna, and E_T is the error due to the laser footprint

not directly striking the reference point. E_{DGPS} can be modeled via information output

from the post-processed GPS data. When averaged over the entire data set, a north error

of 0.0201 m, an east error of 0.0121 m, and an up error of 0.0322 m are present. When

coupled with the lever arm error, the geo-referencing error grows to 0.5644 m, however,

there is still the uncertainty introduced by the laser footprint and truth reference point not

residing at the same location. Unaccounted for is the low data rate of 1 Hz for the

kinematic DGPS truth data resulting in a limited number of data truth points.

Interpolation could possibly be used to upscale the truth data to eliminate some of this

error caused by a low data rate. Results of geo-referencing, including error sources on the

truth data are given in Table 5.1. Figure 5.1 demonstrates both geo-referencing accuracy

and error sources associated with evaluating such accuracy, such as the frequency of the

truth data and the spacing between the truth data and the ALS measurements.

Table 5.1

ALS Footprint Geo-referencing Accuracy Estimation

ALS Footprint Geo-referencing Accuracy								
Runway Fly-over Number	**ALS**	**Lever Arm + DGPS Error (meters)**	**Truth/ Measured Footprint Alignment Error**	**Time of Truth Reference (seconds)**	**Time of Measured Footprint (seconds)**	**Location of Truth Reference (meters)**	**Location of Measured Footprint (meters)**	**Geo-referencing Best Error Estimate (meters)**
1	Fore	0.5644 m	Unknown	423800	423800.1	N=45.0958 E=69.9020 U=0.2780	N=44.7938 E=70.4727 U=-0.5858	1.0785
1	Down	0.5644 m	Unknown	423803	423802.6	N=23.2863 E=30.9030 U=0.1169	N=24.4904 E=32.3063 U=-1.0371	2.1796
2	Fore	0.5644 m	Unknown	424133	424132.6	E=244.9281 N=339.9178 U=-0.04530	E=240.7657 N=333.1888 U=-0.8868	7.9569
2	Down	0.5644 m	Unknown	424134	424133.8	N=255.8571 E=359.2763 U=-0.0526	N=254.7611 E=355.2587 U=-0.5584	4.1950
3	Fore	0.5644 m	Unknown	424574	424574.1	N=-91.3641 E=-218.1012 U=0.4169	N=-91.7913 E=-218.0127 U=-0.8884	1.5704
3	Down	0.5644 m	Unknown	424576	424576.2	N=-91.1722 E=-238.1872 U=0.2909	N=-92.0408 E=-239.1089 U=-0.0288	1.3062
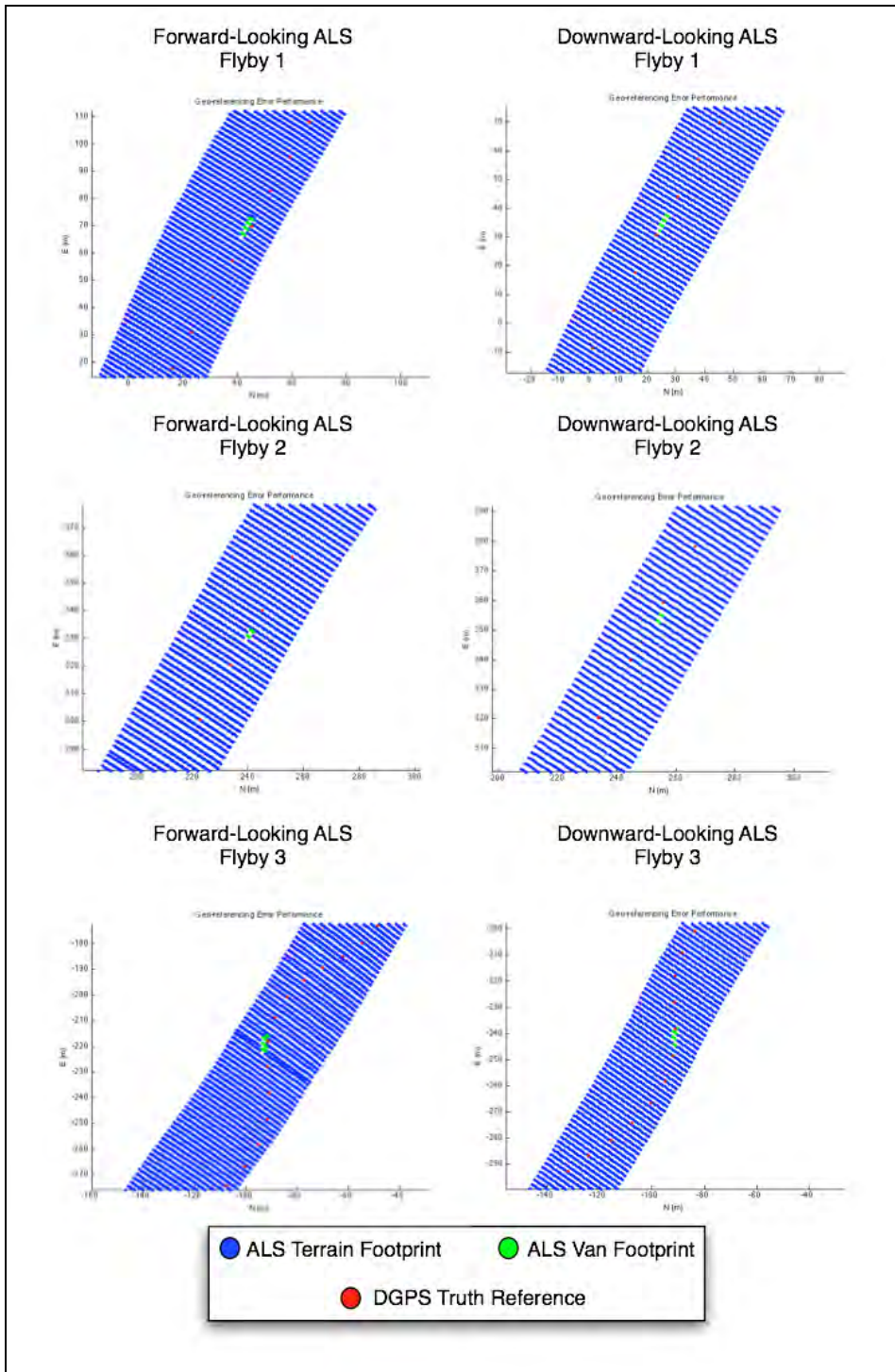
Figure 5.1: Geo-referencing Accuracy Estimation Difficulties Example

Another method used to evaluate the geo-referencing performance uses a comparison of measurements between ALS sensors looking at the same location. By making use of the returned signal intensity value from the laser, it is possible to distinguish unique locations on the runway. The numbers painted on the runway return a unique signal amplitude that can be seen in the surface maps generated by the ALS. The coordinates of the upper right most point of the number seven painted on the runway serves as the reference point for this research. This method still suffers from errors since there is no way to guarantee that the ALS will strike the exact same location on the runway. Table 5.2 details precision results using this method, while Figure 5.2 illustrates the reference point.
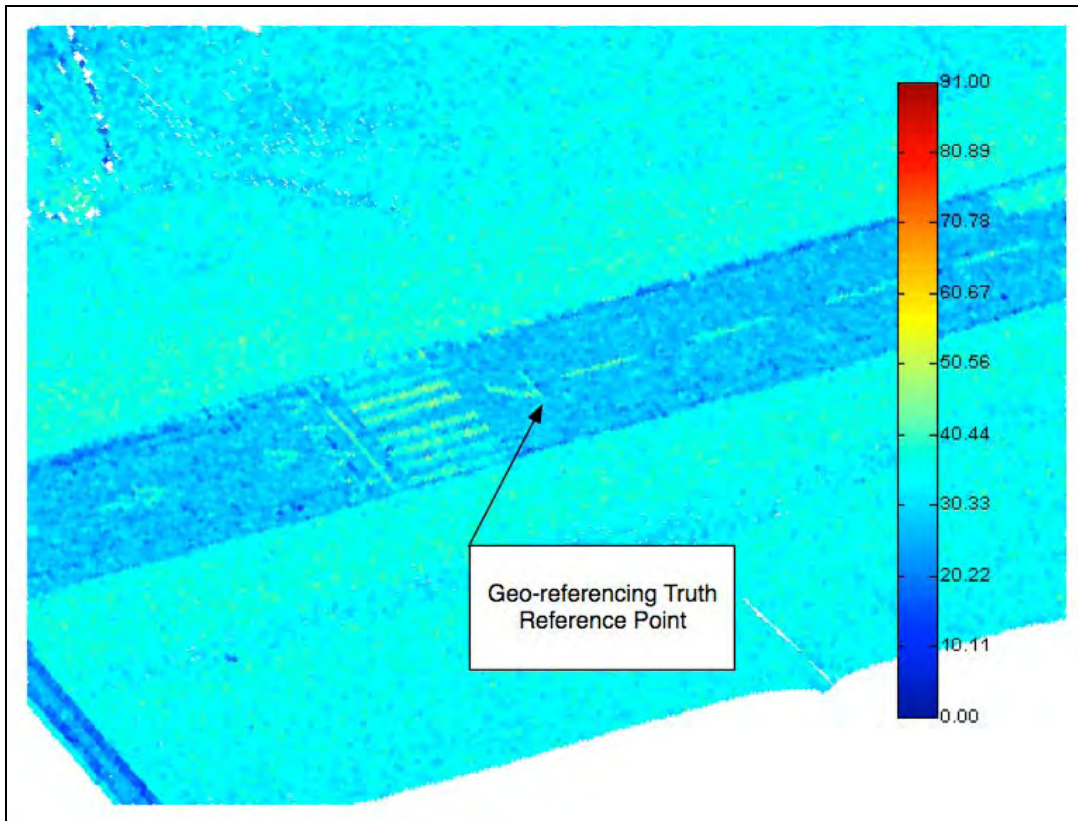
Figure 5.2: Truth reference point used to evaluate geo-referencing precision

Table 5.2

Geo-referencing Precision using ALS Amplitude on Runway Number Truth Reference Point

Fly-over Number	Forward ALS Footprint (ECEF)	Downward ALS Footprint (ECEF)	Footprint Location Difference Forward to Downward (meters)	Footprint Standard Deviation using All Measurements
1	X=668699.3344 Y=-4903409.0721 Z=4010506.4050	X=668698.1651 Y=-4903408.7078 Z=4010507.7131	1.4237	
2	X=668698.1031 Y=-4903409.3740 Z=4010506.2792	X=668697.5442 Y=-4903409.0643 Z=4010507.4294	1.3158	0.5414
3	X=66899.5592 Y=-4903409.4760 Z=4010505.8402	X=668697.7974 Y=-4903409.6281 Z=4010506.8052	2.0145	

5.2 Hazard Detection

The windowed weighted least squares algorithm used for classification of terrain and non-terrain points as well as the k-means clustering performs very well over the runway surface. The method used to evaluate the accuracy of such a procedure is accomplished by plotting the kinematic DGPS of the van position on top of the scene maps created by the ALS. A visual inspection of the data is then preformed along the DGPS van path, in search for a grouping of points residing above the runway surface. Once the hazard candidate is found in the point cloud, the time tag information of the suspected ALS

points is compared with the time-tag of the DGPS van position. The hazard candidate is

verified to be the van if the time data coincides.

When examining the results of the weighted least squares algorithm on each window of

data, it is important to examine the intermediate steps of the algorithm. Figure 5.3 and

Figure 5.4 demonstrate the results of the initial best fit of a 3-D plane though the window,

the determination of the standard deviation of the height residuals, the calculation of the

standard deviation of the residual histogram, and the result of the terrain and non-terrain

point classification.
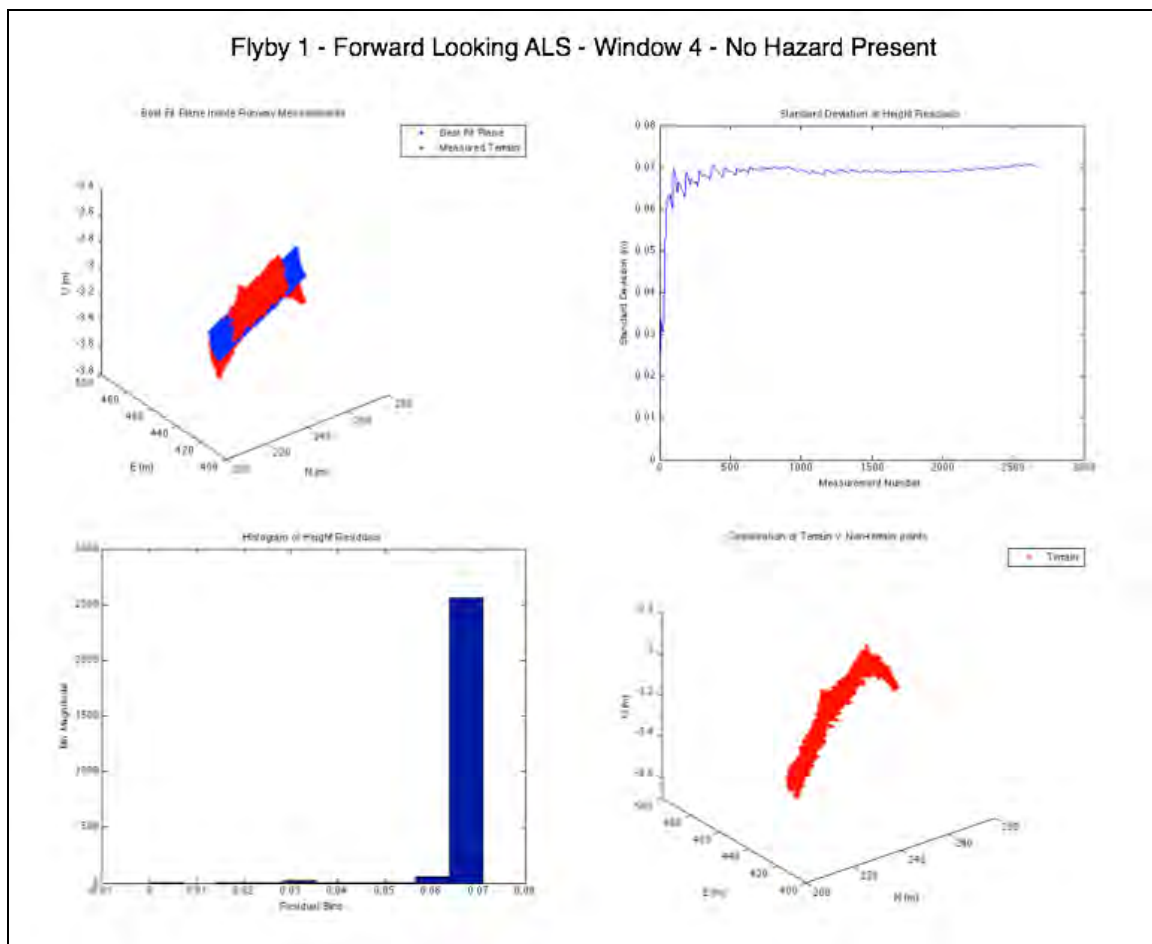
Figure 5.3: Intermediate steps of the weighted least squares algorithm - data window 4 in the forward-looking ALS during fly-over 1 – no hazard present
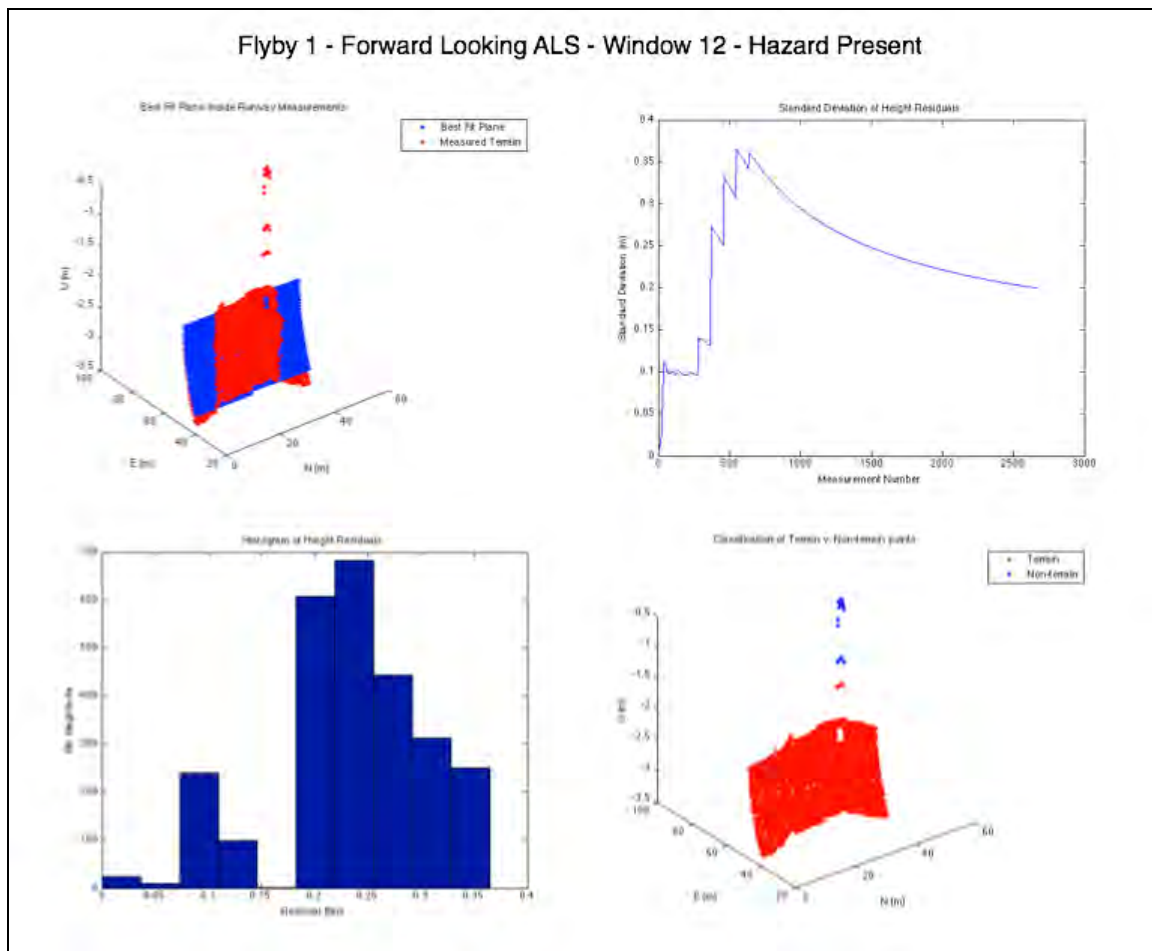
Figure 5.4: Intermediate steps of the weighted least squares algorithm - data window 12 in the forward-looking ALS during fly-over 1 – hazard present

The point cloud window of Figure 5.3 shows that no hazard candidates are present. This is expected since the standard deviation of the residual heights from the best–fit plane fitting are consistent, as can be seen from the shape of the histogram. Window statistics of this realization indicate that no non-terrain points are present, and thus no hazards. Figure 5.4 shows just the opposite. There is a variation in the residual heights as apparent in the regional histogram, implying the existence of a hazard. Figure 5.5 through Figure

5.10 show the results of the algorithm applied over the entire scene map made up of all

windows created during each fly-over.
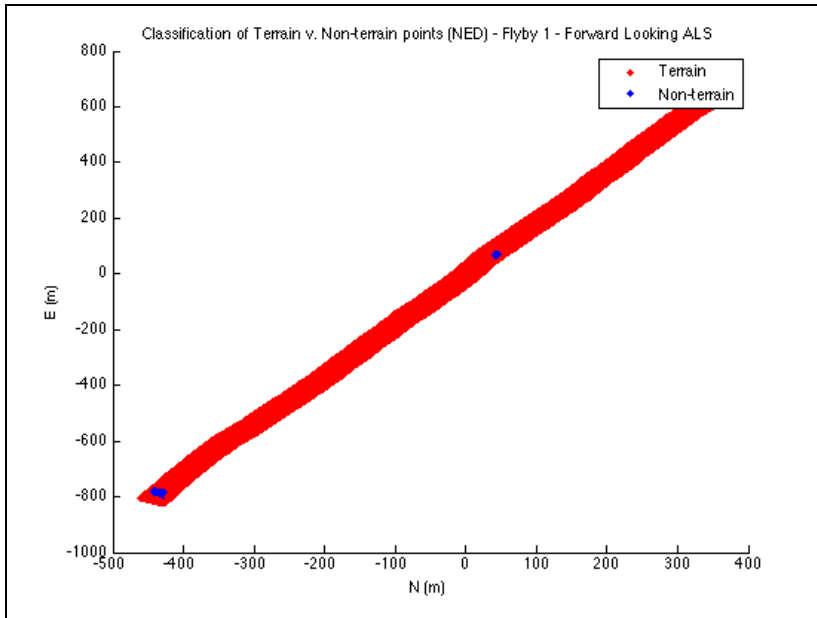
Figure 5.5: Point classification results – fly-over 1 – forward-looking ALS
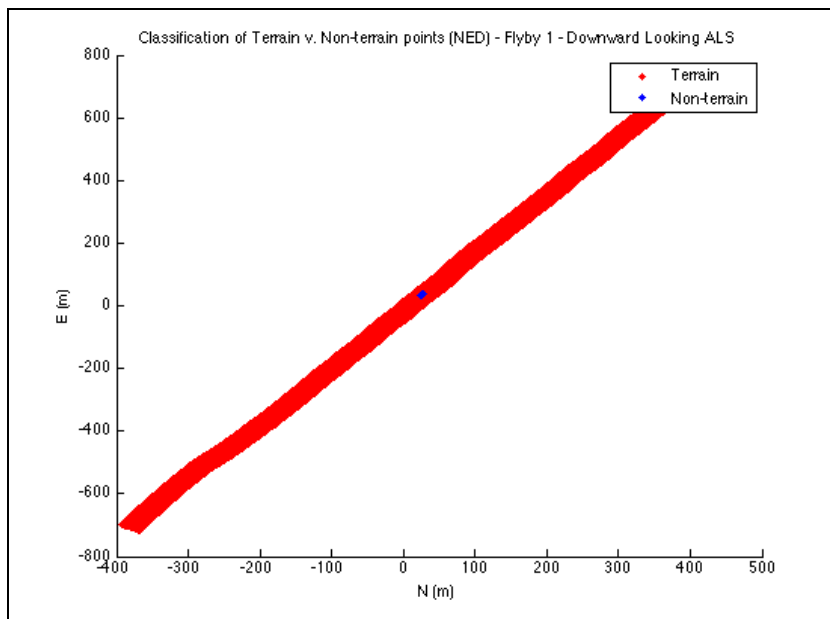
Figure 5.6: Point classification results – fly-over 1 – downward-looking ALS
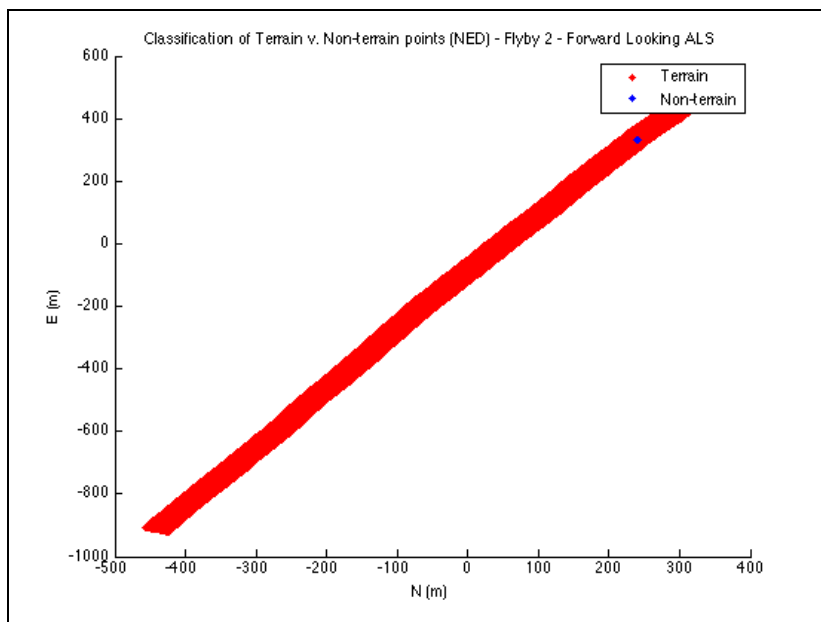
Figure 5.7: Point classification results – fly-over 2 – forward-looking ALS
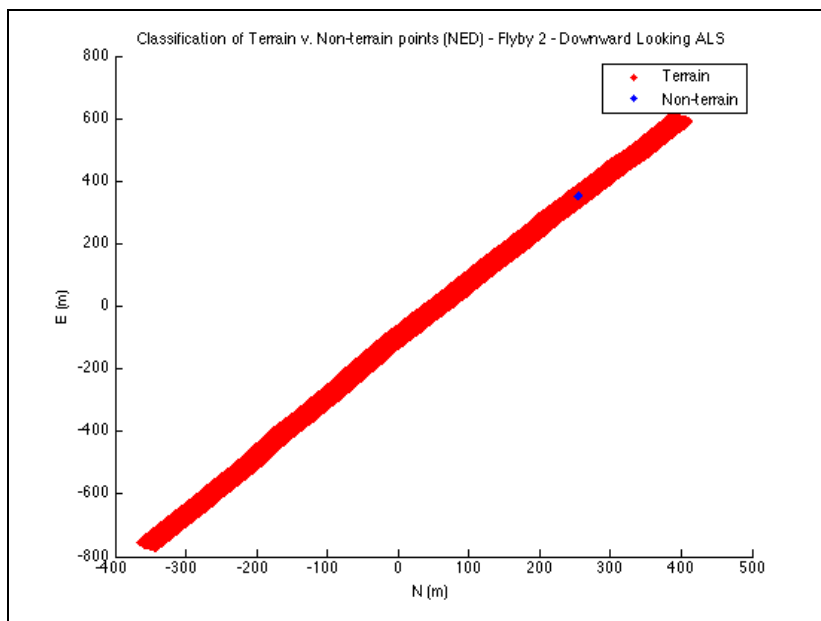
Figure 5.8: Point classification results – fly-over 2 – downward-looking ALS
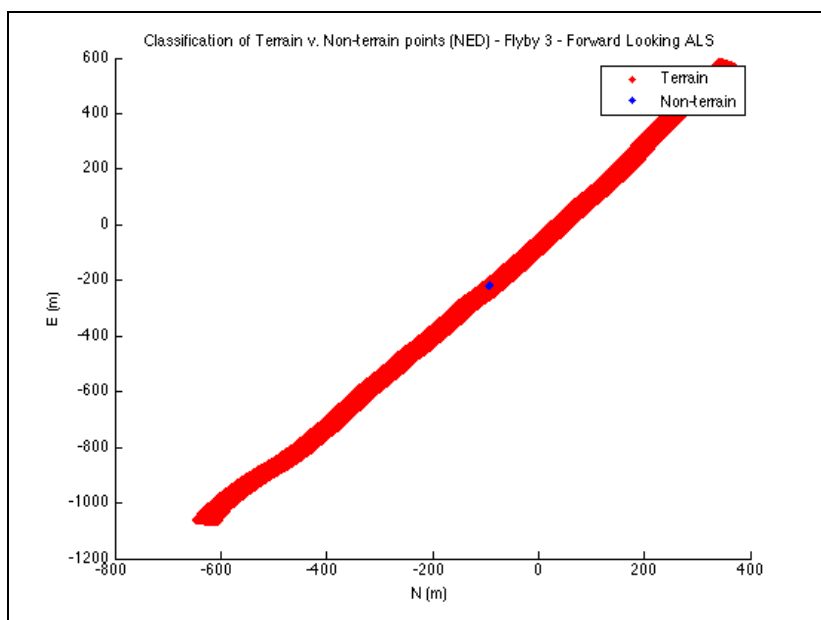
Figure 5.9: Point classification results – fly-over 3 – forward-looking ALS
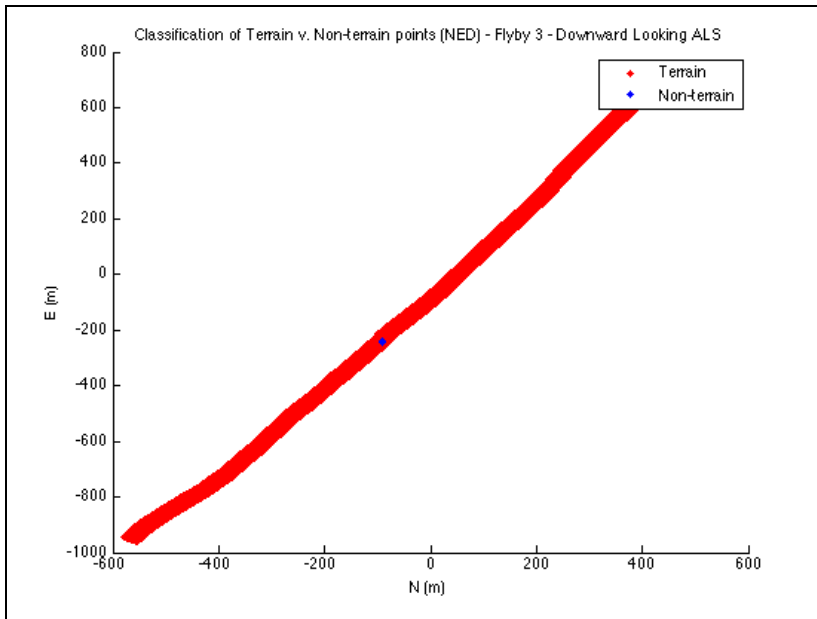
Figure 5.10: Point classification results – fly-over 3 – downward-looking ALS

The above figures illustrate the windowed weighted least squares point classification

algorithm's performs reliably over the runway. In five of the six data sets there are no

false detections and the van is detected correctly each time. There is a false detection in

Figure 5.5 of the forward-looking ALS data of fly-over one, however, the false detection

does not occur on the smooth runway surface, it occurs on the rough terrain encountered

before the start of the runway. This false detection is expected due to the planar fitting

techniques used in this algorithm.

After non-terrain points have been identified they are clustered into sets of points likely

belonging to the same feature. Clustering becomes necessary in multiple-hazard scenarios

to distinguish individual scene features from one another. It is also useful when

determining the size of a non-terrain feature. A cluster consisting of only one or two points may be an artifact or a negligible feature that does not pose a threat to the safety of the aircraft. Figure 5.11 shows the results of clustering the non-terrain points into a single hazard, while Figure 5.12 shows the identification of multiple hazard clusters in a single scene.
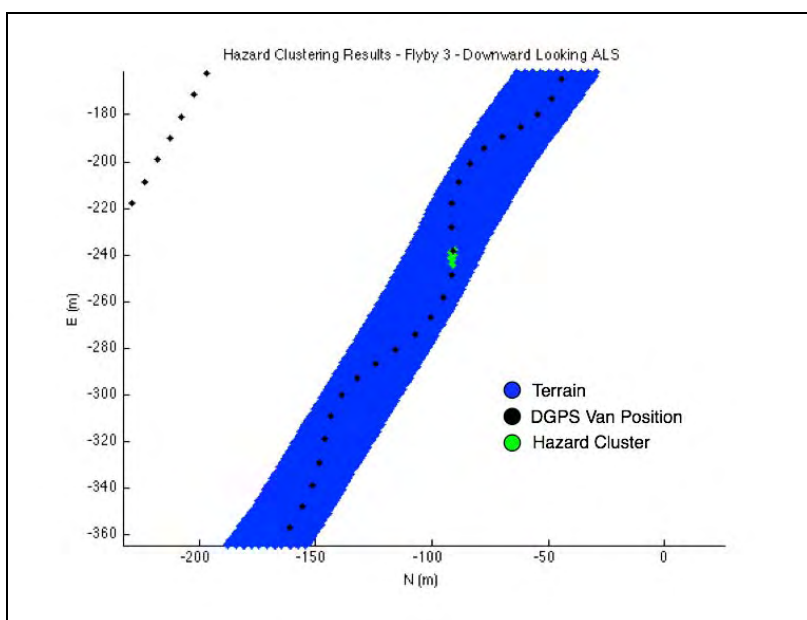
Figure 5.11: Hazard clustering results for the downward-looking ALS of fly-over 3
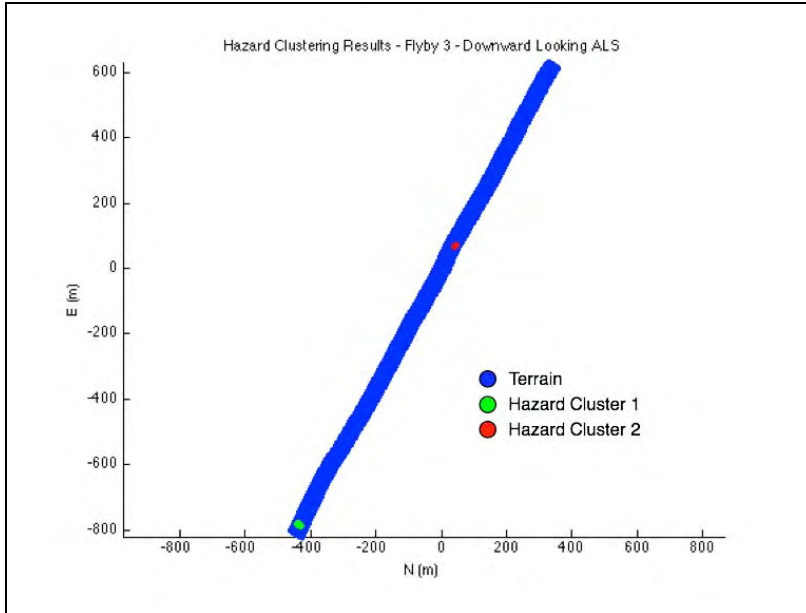
Figure 5.12: Hazard clustering results of multiple hazards for the forward-looking ALS of fly-over 1

Integration of data from both ALS systems after application of the *k*-means clustering algorithm of each fly-over is provided in Figure 5.13 through Figure 5.15. The forward-looking LMS-Q280i ALS yields a larger number of measurements per hazard due increased measurement density caused by the 15° smaller scan width of the LMS-Q280i ALS at a pulse repetition rate identical to that of the LMS-Q140i.
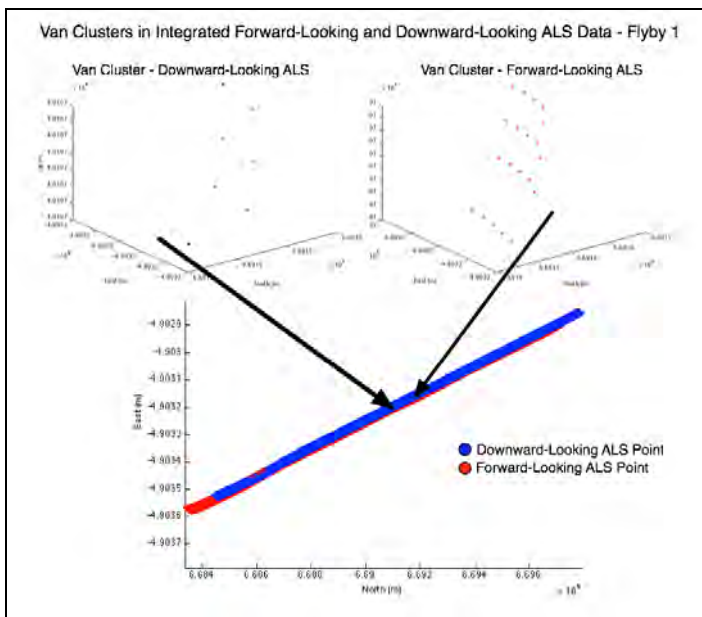
Figure 5.13: Integration of dual ALS data and cluster identification – fly-over 1
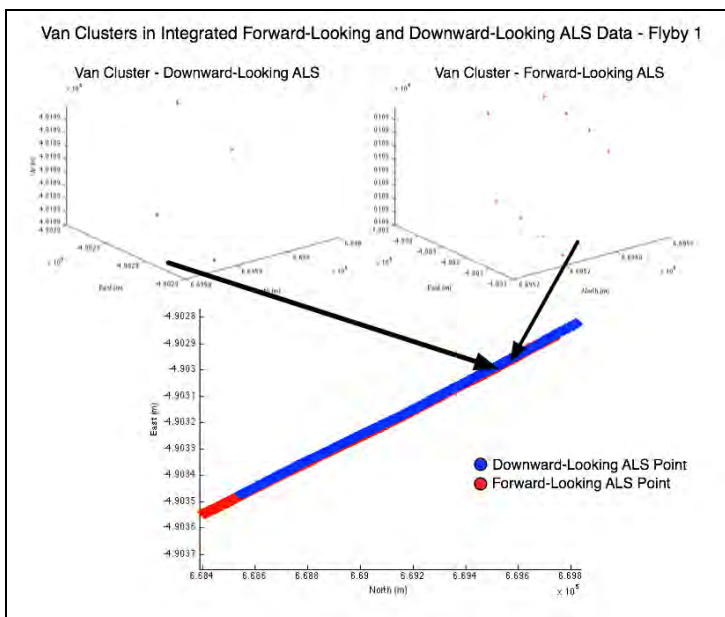
Figure 5.14: Integration of dual ALS data and cluster identification – fly-over 2
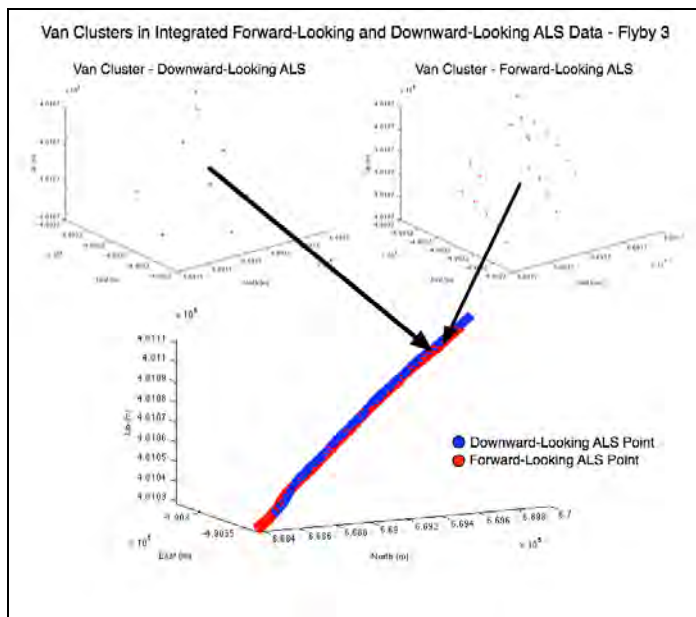
Figure 5.15: Integration of dual ALS data and cluster identification – fly-over 3

5.3 Hazard State Estimation

Upon completion of footprint geo-referencing, point classification, and hazard clustering, the velocity state of the hazard can be calculated. Table 5.3 details all information necessary to estimate hazard average velocity along with the results of such a procedure. As expected, the linear motion of the hazards during fly-over one and two was estimated to within 1.1 m/s of the true van average velocity provided by the kinematic DGPS receiver located inside the van. That error could likely be further improved if there was a method to guarantee that the van remained at a constant speed during the fly-over, however, there were likely small variations in the van's velocity. The non-linear motion of the van on the runway during fly-over three leads to less accurate velocity estimates

since the algorithm used herein relies on the assumption of linear motion. Even in the

presence of non-linear motion the results are promising, providing an average velocity

estimate accurate to within 2.84 m/s. The oblong shape of the runway provides an

advantage in a non-linear motion state since non-linear motion of the van is bounded by

the short distance between runway edge lines.

Table 5.3

Hazard Velocity State Estimation Results

Hazard State Estimation Results				
Fly-over	Time ALS$_D$ (GPS Time of Week)	Cluster Center ALS$_D$ (ECEF)	Time ALS$_F$ (GPS Time of Week)	Cluster Center ALS$_F$ (ECEF)
1	423802.689	X=669148.02 Y=-4903176.53 Z=4010718.59	423800.072	X=6691824.89 Y=-4903159.77 Z=401732.91
2	424133.771	X=424133.77 Y=-4902945.17 Z=4010925.90	424132.576	X=669575.39 Y=-4902956.37 Z=4010914.96
3	424576.166	X=669149.05 Y=-4903172 Z=4010723.53	424574.106	X=669170.97 Y=-4903169.26 Z=4010722.32
Fly-over	Distance (m)	Estimated Van Speed (m/s)	True Van Speed (m/s)	Error (m/s)
1	40.91	15.63	14.52	1.11
2	26.20	21.92	21.77	0.15
3	22.13	10.75	7.91	2.84

CHAPTER 6: CONCLUSIONS

6.1 Summary

The methods and experimental procedure used to detect mobile runway hazards in this research have resulted in a successful proof-of-concept for a system such as NASA's IIFD external hazard monitor. Laser footprint geo-referencing has been proven accurate to within approximately 2 m in most cases. This accuracy is likely much better than the numbers indicated in the results, however, acquisition of truth data and development of precise methods to assess performance has proven difficult. It has been shown that geo-referencing accuracy can only be evaluated to within an unknown tolerance greater than 0.5 m due to factors such as instrument accuracy, lever arm length, and ability of the ALS to directly strike the reference location. Geo-referencing measurement precision of better than 1.5 m in two of the three runway fly-overs provides further assurance that the procedure is more accurate than the results indicate. Hazard identification is near perfect, with only a single false detection, which is the result of jagged terrain located in front of the runway, among all data. Average velocity estimation results of the van are also promising. During linear van motion the velocity is successfully estimated to within 1.2 m/s. Even when the van is driving in a non-linear zigzag pattern, the velocity is calculated to within 2.9 m/s of the truth-value.

The advantages of the proposed system include, high resolution geo-referenced 3-D scene imagery, the ability to detect non-cooperative targets including wildlife, pedestrians, debris, and some ground vehicles, and direct pilot notification of hazards that is

independent of intermediate parties such as ATC. Replacing GPS with a navigation system completely internal to the aircraft such as the dual ALS aided inertial system proposed in [7] would eliminate reliance on any external device, resulting in a hazard monitor capable of operating in environments experiencing RF interference or little or no GPS signal availability. Such a system is more cost feasible to include on an aircraft if the sensors are being used for other flight critical systems as in the dual ALS aided inertial navigation system mentioned above.

6.2 Challenges

The promising performance of the proposed aircraft external hazard monitor demonstrates the effectiveness of this proof-of-concept implementation, however, various factors limiting the system design and flight test experiments have room for improvement that may lead to increased overall system accuracy. The mounting angles and location of both ALSs, selected based on installation cost, were not ideal. Moving the sensors to the nose of the aircraft and pointing both of them forward at different angles would allow the system to detect hazards well before the aircraft flies over them. Increasing the 30.5° separation angle of the lasers would allow for more time between ALS hazard detection, yielding a better average velocity estimate. Another significant improvement to the accuracy of the system, excluded due to measurement cost, would be compensation for the orientation offset between the IMU and each ALS. While this offset is small, it can still lead to considerable footprint geo-referencing errors since ALS range measurements are so large. Increased point density of the downward-looking LMS-Q140i ALS is also

desirable, since as little as four laser pulses struck the van hazard during fly-over two. Decreasing the sweep angle of the ALS could provide a simple fix to this problem; however, replacing the LMS-Q140i with a more advanced ALS such as the LMS-Q280i would be a more effective solution. A final challenge of this research, again limited by cost, was the low number of data collection trials and scenarios. An ideal experiment would include more trials with the van moving in different patterns and directions, such as laterally or stopping and starting. Also included would be a fly-over of the van while it remains stationary with various surveyed reference points along the roof and sides. This would allow for better accuracy assessment. Finally adding a system integrity component, currently missing for this research, would increase both confidence and usefulness with regards to the hazard monitor.

6.3 Looking Forward

This section provides recommendations for future improvements and research pertaining to the dual ALS aircraft external hazard monitor.

- Integration of the returned LIDAR signal's amplitude into the classification and detection algorithms may be used to provide more advanced hazard classification and eliminate false detections. Results from this research indicate that even slight variations in materials comprising scene feature yields unique amplitude signatures that may be integrated into classification data.

- An under utilized sensor included in the initial design of the hazard monitor is the RGB camera. The time-tagged camera data may be fused with the ALS, GPS, and IMU data to provide more integrity to hazard detection and classification.

Segmentation of camera images though image enhancement and edge detection could possibly be used to calculate a heading estimate of the hazard by analyzing the hazard's orientation between the runway edge lines. While vulnerable to darkness, this sensor could be used to provide integrity in numerous landing scenarios.

- An investigation into multiple mobile hazard scenarios to guarantee that each ALS is detecting and estimating the state of the same hazard would prove useful. This could be accomplished by looking for a specific hazard in only a certain area of the scene determined by the location of the hazard in the forward most looking ALS and the aircraft dynamics.

- A final improvement to the research would be further flight-testing to analyze more mobile hazards scenarios. These may include different driving patterns of the van as well as the inclusion of other mobile hazards on the runway such as debris, wildlife, pedestrians, and other aircraft.

- Evaluation of other sensors for external hazard monitoring such as flash LIDAR, and gimbaled ALS sensors.

REFERENCES

[1] D. Jones, C. C. Quach, and S. D. Young, "Runway incursion prevention system –
     demonstration and testing at the Dallas/Fort Worth International Airport," in
     Proceedings of The 21st Digital Avionics Systems Conference, 2002, pp. 2.D.2-
     1-2.D.2-11.

[2] T. Williamson and N. Spencer, "Development and operation of the traffic alert and
     collision avoidance system (TCAS)," in *Proceedings of the IEEE*, 1989, pp.
     1735-1744.

[3] M. Watnick and J. W. Ianniello, "Airport movement area safety system," in
     Proceedings of IEEE/AIAA 11th Digital Avionics Systems Conference, 1992,
     pp. 549-552.

[4] United States of America. Joint Planning and Development Office. *Operation
     Concept for the Next Generation Air Transportation System*, Washington D.
     C., Joint Planning and Development Office, 2007.

[5] M. Smearcheck, A. Vadlamani, and M. Uijt de Haag, "Sensor classification and
     obstacle detection for aircraft external hazard monitoring," in *Proceedings of
     SPIE Vol. 6597, Enhanced and Synthetic Vision 2008*, 2008.

[6] A. Vadlamani, M. Smearcheck, M. Uijt de Haag, "Preliminary design and analysis
     of a LIDAR based obstacle detection system," in *Proceedings of The 24th
     Digital Avionics Systems Conference*, 2005, pp. 6.B.2-61-14.

[7] A. Vadlamani and M. Uijt de Haag, "Aerial vehicle navigation over unknown
     terrain environments using inertial measurements and dual airborne laser

scanners or flash lidar," in *Proceedings of SPIE Vol. 6550, Laser Radar Technology XII*, 2007.

[8] D. Venable, J. Campbell, and M. Uijt de Haag, "Feature extraction and separation in airborne laser scanner terrain integrity monitors," in *Proceedings of The 24th Digital Avionics Systems Conference*, 2005, pp. 4.E.3-41-11.

[9] "Runway Safety Report 2007," Federal Aviation Administration, Washington D. C., United States of America, Tech. Rep., 2007.

[10] "Runway Safety Blueprint 2002-2004," Federal Aviation Administration, Washington D. C., United States of America, Tech. Rep., 2002.

[11] "Runway Incursion Airport Assessment December 2002," Federal Aviation Administration, Washington D. C., United States, Tech Rep., 2002.

[12] National Transportation Safety Board, "Improve Runway Safety," *Most Wanted Transportation Safety Improvements: Federal Issues*, National Transportation Safety Board, 2007. [Online]. Available: http://www.ntsb.gov/recs/mostwanted/runways.htm. [Accessed Dec. 5, 2007].

[13] J. L. Farrell, E. D. McConkey, and C. G. Stephens, "Send measurements, not coordinates," *Journal of the Institute on Navigation*, vol. 64, no. 3, pp. 203-215, 1999.

[14] D. F. Green, "Runway safety monitor algorithm for runway incursion detection and alerting," Lockheed Martin Corporation, Virginia, United States, Tech. Rep., NASA/CR-2002-211416, 2002.

[15] M. Uijt de Haag, J. Sayre, J. Campbell, S. Young, and R. Gray, "Flight test results of a synthetic vision elevation database integrity monitor," in *Proceedings of SPIE Vol. 4363, Enhanced and Synthetic Vision 2001*, 2001, pp. 124-133.

[16] National Transportation Safety Board, "Public meeting of June 13, 2000: Safety Recommendation to the Federal Aviation Administration to prevent runway incursions," *National Transportation Safety Board*, 2000. [Online]. Available: http://www.ntsb.gov/Pressrel/2000/000613.htm. [Accessed Apr. 11, 2008].

[17] G. Go and J. W. Ianniello, "Third generation airport surface detection equipment design," in *Proceedings of The IEEE/ National Aerospace and Electronics Conference*, 1994, pp. 1301-1308.

[18] V. Edwards and C. Evers, "Loop technology (LOT) as an alternative surface surveillance system," in *Proceedings of The 18th Digital Avionics Systems Conference*, 1998, pp. 5.D.1-1-5.D.1-8.

[19] R. Cassell, "Application of PathProx runway incursion alerting to general aviation operations," in *Proceedings of The 24th Digital Avionics Systems Conference*, 2005, pp. 4.D.5-4.1-8.

[20] C. Livadas, J. Lygeros, and N. A. Lynch, "High-level modeling and analysis of the traffic alert and collisionavoidance system (TCAS)," in *Proceedings of the 20th Annual IEEE Real-Time Systems Symposium*, 2000, pp. 926-948.

[21] Australian Transportation Safety Board, "The hazard posed to aircraft by birds," Department of Transportation and Regional Services, Australia, Tech. Rep., 2003.

[22] L. A. Klein, *Sensor and Data Fusion Concepts and Applications.* Bellingham, WA: SPIE Optical Engineering Press, 1999, pp. 7-40.

[23] G D. Hines, Z. Rahman, D. J. Johnson, G. A. Woodell, and S. D. Harrah, "Real-time enhanced vision system," in *Proceedings of SPIE Vol. 5802, Enhanced and Synthetic Vision 2005*, 2005. pp. 127-134.

[24] D. A. Fay, A. M. Waxman, M. Aguilar, D. B. Ireland, J. P. Racamato, W. D. Ross, W. W. Streilein, and M. I. Braun, "Fusion of multi-sensor imagery for night vision: color visualization, target learning, and search," in *Proceedings of the Third International Conference on Information Fusion*, 2000, pp. TUD3/3-TUD310.

[25] D. M. Williams, M. C. Waller, J. H. Koelling, D. W. Burdette, W. R. Carpon, J. S. Barry, R. B. Gifford, and T. M. Doyle, "Concept of operations for commercial and business aircraft synthetic vision systems," NASA Langley Research Center, Virginia, United States of America, Tech. Rep., NASA/TM-2001-211058, 2001.

[26] D. P. Chi Nguyen, S. D. Harrah, and W. R. Jones, "Flight test of IR sensors on NASA 757 at Newport News/ Williamsburg International Airport (PHF)," in *Proceedings of The 21st Digital Avionics Systems Conference*, 2002, pp. 11D6-1-11D6-12.

[27] A. Yilmaz, K. Shafique, and M. Shah, "Target tracking in airborne forward looking infrared imagery," *Image and Vision Computing Journal*, vol. 21, no. 7, pp. 623-635, 2003.

[28] A.D. Lanterman, M.I. Miller, and D.L. Snyder, "Automatic target recognition via the simulation of infrared scenes" in *Proceedings of the 6th Annual Ground Target Modeling and Validation Conference*, 1995, pp. 195-204.

[29] W. L. Stewart, "Passive millimeter wave imaging considerations for tactical aircraft," in *Proceedings of The 20th Digital Avionics Systems Conference*, 2001, pp. 2B2/1-2B2/8.

[30] A.Y. Nashahibi and F.T. Ulaby, "Detection of stationary foliage-obscured targets by polarimetric millimeter-wave radar," *IEEE Transactions on Geoscience and Remote Sensing*, vol. 43, no. 1, pp. 13-23, Jan. 2005.

[31] K. Kaliyaperumal, S. Lakshmanan, and K. Kludge, "An algorithm for detecting roads and obstacles in radar images" *IEEE Transactions on Vehicular Technology*, vol. 50, no. 1, pp. 170-182, Jan. 2001.

[32] N. Gopalsami and A. Raptis, "Millimeter-wave radar sensing of airborne chemicals," *IEEE Transactions on Microwave Theory and Techniques,* vol. 49, no. 4, pp. 646-653, Apr. 2001.

[33] K. Sarabandi and M. Park, "A radar cross-section model for power lines at millimeter wave frequencies," *IEEE Transactions on Antennas and Propagation,* vol. 51, no. 9, pp. 2353-2360, Sept. 2003.

[34] J. B. Mead, A. L. Pazmany, S. M. Sekelsky, and R. E. McIntosh, "Millimeter-wave radars for remotely sensing clouds and precipitation," *Proceedings of IEEE*, vol. 82, no. 12, pp. 1891-1906, 1994.

[35] L. Chen, T. Teo, Y. Lai, and J. Rau, "Fusion of lidar data and optical imagery for building modeling," *International Archives of Photogrammetry and Remote Sensing*, vol. 35, no. B4, pp. 732-737, 2004.

[36] V. J. Norris, R. S. Evans, and D. G. Currie, "Performance comparison of visual infrared, and ultraviolet sensors for landing aircraft in fog," in *Proceedings of the 18th Digital Avionics Systems Conference*, 1999, pp. 5.D.2-1-5.D.2-19.

[37] J. M. Suiter and M. B. Lapis, "Multispectral image fusion for the small aircraft transportation system," in *Proceedings of the 23rd Digital Avionics Systems Conference*, 2004, pp. 4.B.4-41-13.

[38] P. Trisiripisal, M. Parks, A. Abbott, T. Liu, and G. Flemming, "Stereo analysis for vision-based guidance and control of aircraft landing," in *Proceedings of the 44th AIAA Aerospace Sciences Meeting and Exhibit*, 2006.

[39] J. Kim and S. Sukkarieh, "Real-time implementation of airborne inertial-SLAM," *Robotics and Autonomous Systems*, vol. 55, pp. 62-71, 2007.

[40] A. A. Farag and A. E. Abdel-Hakim, "Detection, categorization, and recognition of road signs for autonomous navigation," in *Proceedings of advanced concepts for intelligent vision systems*," pp. 125-130, 2004.

[41] Swiss Ranger, "Swiss ranger SR-3000 datasheet," Swiss Ranger, 2006.

[42] S. May, B. Werner, H. Surmann, and K. Pervölz, "3D time-of-flight cameras for mobile robotics," in *Proceedings of IEEE/RSJ International Conference on Intelligent Robotics and Systems*, 2006, pp. 790-795.

[43] J. L. Campbell, M. M. Miller, M. Uijt de Haag, D. Venable, and M. Smearcheck, "Flash-LIDAR inertial navigator aiding," in *Proceedings of IEEE/ION Position, Location, and Navigation Symposium*, 2006, pp. 677-683.

[44] B. Hanna, B. Chai, and S. Hsu, "Wide-area terrain mapping by registration of flash LIDAR imagery," in *Proceedings of SPIE Vol. 5791, Laser Radar Technology*, 2005, pp. 193-207.

[45] J. M. Trenkle, P. Tchoryk, G. A. Ritter, J. C. Pavlich, and A. S. Hickerson, "3-D sensors algorithm for spacecraft pose estimation," in *Proceedings of SPIE Vol. 6220, Spaceborne Sensors III*, 2006.

[46] A. Vydhyanathan, "Effect of atmospheric particulates on airborne laser scanning for terrain-referenced navigation," M.S. thesis, Ohio University, Athens, OH, United States of America, 2006.

[47] R. L. Associates, "NASA NIR EHD," *R. L. Associates*. [Online]. Available: http://rlassociatesinc.com/nir.html [Accessed Apr. 5, 2008].

[48] K. Zhang, S. Chen, D. Whitman, M. Shyu, J. Yan, and C. Zhang, "A progressive morphological filter for removing nonground measurements from airborne LIDAR data," *IEEE Transactions on Geoscience and Remote Sensing*, vol. 41, no. 4, pp. 872-882, Apr. 2003.

[49] F. Rottensteiner and J. Jansa, "Automatic extraction of buildings from LIDAR data and aerial images," In *Proceedings of the 21st International Society of Photogrammetry and Remote Sensing Congress (ISPRS)*, 2002, pp. 569-574.

[50]   C. Toth, D. Grenjner-Brzezinska, E. Paska, and S. Moafipoor, "Precise vehicle topology and road surface modeling derived from airborne LIDAR data," presented at The 60th Annual Meeting of the ION, 2004.

[51]   A. B. Utkin, "Forest-fire detection by means of lidar," in *Proceedings of IV International Conference on Forest Fire Research and Wildland Safety*, 2002.

[52]   D. Titterton and J. Weston, *Strapdown Inertial Navigation Technology*, 2nd ed., Reston: The American Institute of Aeronautics and Astronautics, 2004.

[53]   W. Travis, A. T. Simmons, and D. M. Bevly, "Corridor navigation with a LiDAR/INS Kalman filter solution," in *Proceedings of IEEE Intelligent Vehicles Symposium*, 2005, pp. 343-348.

[54]   Optech International Inc., "ALTM 3100EA," *Opetch International Inc.*, 2006. [Online]. Available: http://www.optech.ca/pdf/Brochures/ALTM3100EAwspecsfnl.pdf [Accessed Feb 14, 2008].

[55]   Advanced Scientific Concepts Inc., "3D IR Visible Bundled System," *Advanced Scientific Concepts Inc.*, 2006. [Online]. Available: http://www.advancedscientificconcepts.com/bundle1.html [Accessed Feb. 12, 2008].

[56]   Prosilica, "GC Series Specifications," Prosilica, 2006. [Online]. Available: http://www.prosilica.com/products/specifications/gc_series_specs.html [Accessed Feb. 15, 2008].

[57] FLIR Government Systems, "Star SAFIRE HD," FLIR Government Systems, 2007. [Online]. Available: http://www.gs.flir.com/docs/gs/Documents/StarSafire_HD.pdf [Accessed Feb. 15, 2008].

[58] ICX Radar Systems, "NASA ERAST Non-Cooperative DSA Flight Test," ICX Radar Systems, 2003. [Online]. Available: http://www.amphitech.com/pdf/mtsi_auvsiconference.pdf [Accessed: Feb. 15, 2008].

[59] M. Kayton and R. Fried, Avionics Navigation Systems, 2nd ed., New York: John & Wiley Sons Inc., 1997.

[60] D. Eberly, "Least squares fitting of data," geometrictools.com, July 2007. [Online]. Available: http://www.geometrictools.com/Documentation/LeastSquaresFitting.pdf. [Accessed Feb. 9, 2008].

[61] G. Strang, *Linear Algebra and its Applications*, 3rd ed., Brooks Cole, 1998.

[62] D. Bates, "Navigation of optical tracking of objects at unknown locations," M.S. thesis, Ohio University, Athens, OH, United States, 2007.

[63] S. Theodoridis and K. Koutroumbas, *Pattern Recognition*, 3rd ed., San Diego: Elsevier, 2006.

[64] F. Morsdorf, E. Meier, B. Allgöwer, and D. Nüesch, "Clustering in airborne laser scanning and raw data for segmentation of single trees," in *Proceedings ISPRS*

Working Group III/3 Workshop 3-D reconstruction from airborne laserscanner and InSAR data Volume 34, 2003, pp. 27-33.

[65] Honeywell, *HG1150BD02 IRU Technical Documentation*, Honeywell Commercial Flight Systems – Minneapolis Operation, 1996.

[66] NovAtel, *OEM4 Family Installation and Operation User Manual*, NovAtel Inc., 2005.

[67] Reigl, *LMS-Q280i Airborne Laser Scanner, Technical Documentation and Users Instructions*, Riegl Laser Measurement Systems, Austria, 2004.

[68] Riegl, *Laser Mirror Scanner LMS-Q140-60-HR, Technical Documentation and Users Instructions*, Riegl Laser Measurement Systems, Austria, 2001.

[69] Prosilica, *User Manual: GC1350/GC1350C*, Prosilica Incorporated, Canada, 2007.

[70] K. Kraus and N. Pfeifer, "Determination of terrain models in wooded areas with airborne laser scanner data," *ISPRS Journal of Photogrammetry and Remote Sensing*, vol. 53, pp. 193-203, 1998.

[71] U. Braga-Neto, M. Choudhary, and J. Goutsias, "Automatic target detection and tracking in forward-looking infrared image sequences using morphological connected operators," *Journal of Electronic Imaging*, vol. 13, no. 4, pp. 802-813, Oct. 2004.

[72] C. Pai, Y. Lin, G.G. Medioni, and R.R. Rida, "Moving object detection on a runway prior to landing using an onboard infrared camera," in *Proceedings of IEEE Conference on Computer Vision and Pattern Recognition*, 2007, pp. 1-8.

[73] A. Yilmaz, K. Shafique, N. Lovo, X. Li, T. Olson, and M.A. Shah, "Target tracking in FLIR imagery using mean-shift and global motion compensation", in *Proceedings of IEEE Workshop on Computer Vision Beyond Vehicle Spectrum*, Hawaii, 2001.

[74] F. Zhang, C. Li, and L. Shi, "Detection and tracking dim moving point target in IR image sequence," *Infrared Physics and Technology*, vol. 46, no. 4, pp. 323-328, Apr. 2005.

[75] A. Tartakovsky, S. Klingys, and A. Petrov, "Adaptive sequential algorithms for detecting targets in a heavy IR clutter," in *Proceedings of SPIE Vol. 3809, Signal and Data Processing of Small Targets*, 1999, pp. 119-130.

[76] T. Aytac and B. Barshan, "Differentiation and localization of targets using infrared sensors," *Optics Communications*, vol. 210, pp. 25-35, Sept. 2002.

[77] F.A. Sadjadi, "Infrared target detection with probability density functions of wavelet transform subbands," *Applied Optics*, vol. 43, no. 2, pp. 315-323, Jan. 2004.

[78] F. Xu, X. Liu, K. Fujimura, "Pedestrian detection and tracking with night vision," IEEE *Transactions of Intelligent Transportation Systems*, vol. 6, no. 1, pp. 63-71, Mar. 2005.

[79] H. Nanda and L.S. Davis, "Probabilistic template based pedestrian detection in infrared videos," presented at the IEEE Intelligent Vehicles Symposium, Versailles, France, 2002.

[80] X. Mei, S.K. Zhou, and H. Wu, "Integrated detection, tracking and recognition for IR video-based vehicle classification," in *Proceedings of. IEEE International Conference of Acoustics, Speech, & Signal Processing*, 2006, pp. 745–748.

[81] C. Martin, S. Clark, J. Galliano, and J. Lovberg, "Advances in millimeter-wave imaging technology for enhanced vision systems," in *Proceedings of the 21st Digital Avionics Systems Conference*, 2002, pp. 11D4-1-11D4-8.

[82] F. Sadjadi, M. Helgeson, J. Radke, and G. Stein, "Radar synthetic vision system for adverse weather aircraft landing," *IEEE Transactions on Aerospace and Electronic Systems*, vol. 35, no. 1, pp. 2-14, Jan. 1999.

[83] G. Brooker, R. Hennessey, M. Bishop, C. Lobsey, and H. Durrent-Whyte, "High-resolution millimeter-wave radar systems for visualization of unstructured outdoor environments," *Journal of Field Robotics*, vol. 23, no. 10, pp. 891-912, 2006.

[84] A. Foessel-Bunting and W. Whittaker, "MMW-scanning radar for descent guidance and landing safeguard," in *Proceedings of the 6th International Symposium on Artificial Intelligence, Robotics, and Automation in Space*, 2001.

[85] B.D. Pollard and G. Sadowy, "Next generation millimeter-wave radar for safe planetary landing," in *Proceedings of IEEE Aerospace Conference*, 2005, pp. 1213-1219.

[86] S. Sull and B. Sridhar, "Runway obstacle detection by controlled spatiotemporal image flow disparity," *IEEE Transactions on Robotics and Automation*, vol. 15, no. 3, pp. 537- 547, June 1999.

[87] D. Meng, C. Yun-feng, and G. Lin, "A method to recognize and track runway in the image sequences based on template matching," in *Proceedings of the 1ˢᵗ International Symposium on Systems and Control in Aerospace and Astronautics*, 2006, pp. 1218-1221.

[88] R. Sattigeri, E. Johnson, A. Calise, and J. Ha, "Vision-based target tracking with adaptive target state estimator," in *Proceedings of the AIAA Guidance, Navigation, and Control Conference*, 2007.

[89] G. B. Ladd, A. Nagchaudhuri, T. J. Earl, M. Mitra, and G. L. Bland, "Rectification, georeferencing, and mosaicking of images acquired with remotely operated aerial platforms," in *Proceedings of American Society for Photogrammetry and Remote Sensing*, 2006.

[90] R. C. Fenton, R. R. Fullmer, and R. T. Pack, "Design of lidar-based sensors and algorithms for determining the relative motion of an impaired spacecraft," in *Proceedings of SPIE Vol. 5778, Sensors, and Command, Control, Communications, and Intelligence Technologies for Homeland Security and Homeland Defense IV*, 2005, pp. 809-818.

[91] A. Gelbart, B. C. Redman, R. S. Light, C. A. Schwartzlow, and A. J. Griffis, "Flash LIDAR based on multiple-slit streak tube imaging LIDAR," in *Proceedings of SPIE Vol. 4723, Laser Radar Technology and Applications VII*, 2002, pp. 9-18.

[92] B.C. Matei, Y. Tan, H.S. Sawhney, and R. Kumar, "Rapid and scalable 3D object recognition using LiDAR data," in *Proceedings of SPIE Vol. 6234, Automatic Target Recognition XVI,* 2006.

[93] R. Morrison, J. T. Turner, M. Barwick, and M. Hardaway, "Urban reconnaissance with an airborne laser radar," in *Proceedings of SPIE Vol. 5791, Laser Radar Technology and Applications X*, 2005.

[94] T. Murray, S. E. Moran, N. Roddier, R. Vercillio, R. Bridges, and W. Austin, "Advanced 3D polarimetric flash ladar imaging through foliage," in *Proceedings of SPIE Vol. 5086, Laser Radar Technology and Applications VIII*, 2003, pp. 84-95.

[95] J.W. Weingarten, G. Gruener, and, R. Siegwart, "A state-of-the-art sensor for robotic navigation," in *Proceedings of IEEE/RSJ International Conference on Intelligent Robots and Systems*, 2004, pp. 2155-2160.

[96] D.W. Opitz, R. Rao, and J.S. Blundell, "Automated 3-D feature extraction from terrestrial and airborne LIDAR," In *Proceedings of the 1st International Conference on Object-Based Image Analysis*, 2006.

[97] S. Clode, P. Kootsookos, and F. Rottensteiner, "The automatic extraction of roads from LIDAR data," *The International Archive of Photogrammetry, Remote Sensing and Spatial Information Sciences*, vol. 35, pp. 231-236, 2004.

[98] R.M. Palenichka and M.B. Zaremba, "Multiscale isotropic matched filtering for individual tree detection in LIDAR images," *IEEE Transactions on Geoscience and Remote Sensing*, vol. 45, no. 12, pp. 3944-3956, Dec. 2007.

[99] A.E. Johnson, A.R. Klumpp, J.B. Collier, and A.A. Wolf, "LIDAR-based hazard avoidance for safe landing on Mars," *Journal of Guidance, Control, and Dynamics*, vol. 25, no. 6, pp. 1091-1099, 2002.

[100] C.E. Parrish, "Analysis of airborne laser-scanning system configurations for detecting airport obstructions," M.S. thesis, University of Florida, Gainesville, Fl, United States, 2003.

[101] C. Briese, N. Pfeifer, and P. Dorninger, "Applications of the robust interpolation for DTM determination," *International Archives of Photogrammetry and Remote Sensing*, vol. 34, pp. 55-61, 2002.

[102] J.E. Means, S.A. Acker, D.J. Harding, J.B. Blair, M.A. Lefsky, W.B. Cohen, M.E. Harmon, and W.A. McKee, "Use of large-footprint scanning airborne LIDAR to estimate forest stand characteristics in the Western Cascades of Oregon," *Remote Sensing of Environment*, vol. 67, pp. 298-308, 1999.

[103] H.S. Lee and N.H. Younan, "DTM extraction of LIDAR returns via adaptive processing," *IEEE Transactions on Geoscience and Remote Sensing*, vol. 41, no. 9, pp. 2063-2069, Sept. 2003.

APPENDIX A: CURRENT RESEARCH AND APPLICATIONS OF AIRBORNE SENSORS

Table A.1

Current Research and Applications of IR

Title	Primary Author/ Organization	Application	Objects Detected or Tracked	Conclusions	Ref. Num.
Automatic target detection and tracking in forward-looking infrared image sequences using morphological connected operators	U. Braga-Neto *University of Texas*	Detection of targets in IR video	Any potential target	Detects temperature invariant targets and removes clutter using morphological operators	[71]
Flight test of IR sensors on NASA 757 at Newport News / Williamsburg International Airport (PHF)	D.P. Chi Nguyen *RTI International*	Uses both SWIR and LWIR in Enhanced Vision System	Entire Scene	Operation parameters and performance of IR for sensing of airport surfaces have been analyzed	[26]
Moving object detection on a runway prior to landing using an onboard infrared camera	C. Pai *University of Southern California*	Identify features by normalizing images and then removing the background	Moving objects on runway	Poor detection of fast moving objects and added noise with large objects	[72]
Target tracking in airborne forward looking infrared imagery	A. Yilmaz *University of Central Florida*	Ego-motion compensated detection and tracking targets using fuzzy clustering and edge fusion	Targets with known parameters	Must know position and size of target. Uses texture information to identify targets Tracking from target center using standard deviation distribution	[27]

Target tracking in FLIR imagery using mean-shift and global motion compensation	A. Yilmaz *University of Central Florid*	Tracking using target intensity Gabor response under sensor ego-motion	Any object of with *a priori* position information	Functions for fast moving objects Able to track only one target	[73]
Detection and tracking dim moving point target in IR image sequence	F. Zhang *Wuham University*	Variation of the track before detect method	Any target with low SNR	Requires pre-processing and linear position vector of object.	[74]
Automatic target recognition via the simulation of infrared scenes	A. Lanterman *Washington University*	Use sensor statistics and emissive values of targets for data simulation	Vehicles	Assumes *a priori* target intensity. Does not function with complex natural backgrounds.	[28]
Adaptive sequential algorithms for detecting targets in a heavy IR clutter	A. Tartakovsky *University of Southern California*	Detection and tracking of targets and target disappearance using the track before detect method	Primarily missiles, but applicable to most targets	Performs well for low SNR. Maximum of one false alarm per minute. Initial detection requires 20 seconds.	[75]
Differentiation and localization of targets using infrared sensors	T. Aytac *Bilkent University*	Identifies targets and determines position with respect to indoor environment	Indoor targets corridor corners, planes, and edges	Successful classification rate of 97%. Localization of targets to within 0.8 cm of range and 1.6° of azimuth.	[76]
Infrared target detection with probability density functions of wavelet transform subbands	F.A. Sadjadi *Lockheed Martin Corporation*	Target detection method makes use of texture information, probability density function, and wavelet decomposition	General targets	Targets are differentiated from background using clustering of probability density function moments. Performance models of such a system are developed based on scene specific parameters.	[77]

Pedestrian detection and tracking with night vision	F. Xu *Leica Geosystem*	Pedestrian detection via support vector machine and tracking with a Kalman filter and mean shift tracking	Pedestrians	Does not guarantee detection in all video frames.	[78]
Probabilistic template based pedestrian detection in infrared videos	H. Nanha *University of Maryland*	Uses a Baysian classifier to determine regions of interest then it performs template matching to detect pedestrians. Templates do not include limbs of pedestrians.	Pedestrians	Successful detection rates between 75% and 90%. Detection algorithm requires training.	[79]
Integrated detection, tracking and recognition for IR video-based vehicle classification	X. Mei *University of Maryland*	Vehicles are detected based on temporal variance analysis and then tracked and classified with probabilistic principle component analysis.	Vehicles	Recognition accuracy near 90%.	[80]

Table A.2

Current Research and Applications of MMWR

Title	Primary Author/ Organization	Application	Objects Detected	Conclusions	Ref. Num.
Advances in millimeter-wave imaging technology for enhanced vision systems	*C. Martin* *Trex Enterprises*	Passive MMW radar for enhanced vision systems	Scenes when landing and taxing	Development of higher resolution and broader field of view flat-panel filled array antenna.	[81]
An algorithm for detecting roads and obstacles in radar images	K. Kaliyaperumal *Motorola*	Detects and classifies roads and obstacles in all-weather conditions	Roads and Obstacles	Successful algorithm based on template matching and the Metropolis algorithm.	[31]
Detection of stationary foliage-obscured targets by polarimetric millimeter-wave radar	A.Y. Nashashibi *University of Michigan*	Detection techniques of distorted and backscattered targets in foliage	Ground targets	Distortion reduction and attenuation estimation of signal through foliage using multiple scans of a target proves for successful detection.	[30]
Radar synthetic vision system for adverse weather aircraft landing	F. Sadjadi *Lockheed Martin Corp.*	Algorithms for processing of MMW radar and FLIR data in zero visibility conditions	Runway scenes	Demonstration of 35 GHz radar in a SVS for safe landing.	[82]
High-resolution millimeter-wave radar systems for visualization of unstructured outdoor environments	G. Brooker *University of Sydney*	Path planning and navigation techniques with MMW radar	Terrain	Presents results of various MMW radars' performance characteristics over terrain.	[83]
MMW-scanning radar for descent guidance and landing safeguard	A. Foessel-Bunting *Carnegie Mellon University*	Use of MMW radar for landing of a spacecraft	Terrain	Provides analysis of spacecraft landing scenarios and requirements of a MMW radar for this application.	[84]

Next generation millimeter-wave radar for safe planetary landing	B.D. Pollard *Jet Propulsion Laboratory*	Use of G-band imager for hazard avoidance in unknown environments	Unknown terrain	Design specifications based on planetary landing are provided.	[85]
A radar cross-section model for power lines at millimeter-wave frequencies	K. Sarabandi *Raytheon*	Analysis of radar return characteristics on various power lines	Power lines	Details scattering properties and sensitivity analysis at 94 GHz.	[33]
Millimeter-wave radar sensing of airborne chemicals	N. Gopalsami *Argonne National Laboratory*	Design of MMW radar for chemical detection in 220-350 GHz range	Airborne Chemicals	Successful testing and model development of sensor. Preliminary results demonstrate effective detection capabilities.	[32]

Table A.3

Current Research and Applications of Video

Title	Primary Author/ Organization	Application	Objects Detected or Tracked	Conclusions	Ref. Num.
Runway obstacle detection by controlled spatiotemporal image flow disparity	S. Sull *Korea University, Seoul (Korea)*	Bare runway is estimated using a model flow field. The residual flow of the sensed runway is used to detect hazards.	Objects located on runway	While not very accurate and computational-ly expensive, the method is effective. Can also be used with ground vehicles.	[86]
A method to recognize and track runway in the image sequences based on template matching	D. Meng *University of Aeronautics and Astronautics (China)*	Application of basic image processing techniques for detection of runways for UAVs	Runways	Algorithm is implemented in real-time and uses little information. Method is simple, but does not appear very reliable.	[87]
Real-time implementation of airborne inertial-SLAM	J. Kim *The Australian National University (Australia)*	Use of simultaneous localization and mapping for UAV guidance.	Terrain features	Attitude errors from the IMU have a large effect on algorithms performance. Adding velocity estimates will likely reduce errors.	[39]
Fusion of lidar data and optical imagery for building modeling	L. Chen *National Central University (Taiwan)*	Uses lidar data to model buildings and augments the process with edge information from optical images.	Buildings	Successful detection of %81 of buildings and sub-meter accuracy when using a stereo pair of cameras.	[35]

Vision-based target tracking with adaptive target state estimator	R. Sattigeri *Georgia Institute of Technology*	An algorithm using a Kalman filter based neural network for tracking aircraft in images.	Aircraft	Developed a simulator that yields promising results.	[88]
Stereo analysis for vision-based guidance and control of aircraft landing	P. Trisiropisal *Virginia Tech*	Landing without *a priori* runway information by estimating runway edges and range using a stereo pair of cameras.	Runways	Accurate performance for runway landings. Runways with fading paint decreased performance.	[38]
Rectification, georeferencing, and mosaicking of images acquired with remotely operated aerial platforms	G. Ladd *University of Maryland*	Aerial mapping and surveillance of fields for farming	Terrain and fields	Images are adjusted combined and the pixels are geo-referenced. Individual fields are also detected.	[89]

Table A.4

Current Research and Applications of flash LIDAR

Title	Primary Author/ Organization	Application	Objects Detected	Conclusions	Ref. Num.
Design of lidar-based sensors and algorithms for determining the relative motion of an impaired spacecraft	R. Fenton *Utah State University*	Relative position and attitude determination for spacecraft docking	Spacecraft	Successful simulation of relative positioning using the Iterative Closest Point algorithm. Alignment initialization of the algorithm is yet to be implemented.	[90]
Flash-LADAR Inertial Navigation Aiding	J. Campbell *Air Force Research Labs*	Navigation	Corridors, building walls	Integration with IMU to determine the difference of common features in two successive scenes is a reliable method for indoor navigation.	[43]
Flash LiDAR based on multiple-slit streak tube imaging LiDAR	A. Gelbart *Areté Associates*	Design and field testing of a flash LiDAR	Vehicle hidden in foliage, underwater mines	Able to achieve frame rates of 100 Hz and range accuracies near 2.5% of the total range.	[91]
Wide-area terrain mapping by registration of flash LiDAR imagery	B. Hanna *Sarnof Corp.*	Coupling with GPS/INS and RGB camera for mapping	Terrain	Deals with large files sizes of DEM, overlapping flights, and combination of data sets.	[44]
Rapid and scalable 3D object recognition using LiDAR data	B. Matei *Sarnof Corp.*	Feature recognition in 3-D laser data by matching with model database	General features	Recognizes 94% of targets. Creation of large model database.	[92]
Urban reconnaissance with an airborne laser radar	R. Morrison *Geospatial Technologies*	Sensor characteristics, data processing, and geo-referencing in reconnaissance using UAVs	Features of interest	An overview of flash LiDAR sensors and processing techniques associated reconnaissance	[93]

Advanced 3D polarmetric flash lidar imaging through foliage	J. Murray *Lite Cycles, Inc.*	Imaging through foliage	Tanks	Preliminary work. Has various environmental factors that are not considered, but suggested.	[94]
A state-of-the-art sensor for robotic navigation	J.W. Weingarten *Swiss Federal Institute of Technology*	Navigation and obstacle avoidance with flash-LiDAR	Corridors, indoor hazards	Results show that the Swiss Ranger Flash LiDAR is well suited for collision avoidance and path planning in robots.	[95]

Table A.5

Current Research and Applications of ALS

Title	Primary Author/ Organization	Application	Objects Detected	Conclusions	Ref. Num.
Automated 3-D feature extraction from terrestrial and airborne LIDAR	D. W. Opitz

VLS Systems Inc. | Developed commercial software for rapid 3D feature extraction in urban areas. | Buildings, Roads, Airport Features, Trees | Software extracts over 1,000 buildings per minute with greater than 95% accuracy.

Bare Earth model generation with almost all of the error attributed to the sensor itself. | [96] |
| Automatic extraction of buildings from LIDAR data and aerial images | F. Rottensteiner

Vienna University of Technology (Austria) | Building extraction from point cloud data. | Buildings | Combining visible light imagery with LIDAR data to create building models. Extraction performance metrics have also been developed. | [49] |
| The automatic extraction of roads from LIDAR data | S. Clode

The University of Queensland (Australia) | Road extraction via airborne laser range and intensity data. | Roads | Makes the assumption that roads lie close to self generated DTM values. The DTM is a product of the filtered DSM.

Difficulties when the roads contain cars. | [97] |
| Multiscale isotropic matched filtering for individual tree detection in LIDAR images | R. M. Palenichka

Université du Québec (Canada) | Tree detection and extraction. | Trees | Method does not depend on tree crown height, image resolution, tree density, or external DTMs. | [98] |

A progressive morphological filter for removing nonground measurements from airborne LIDAR data	K. Zhang *Florida International University*	Detection, classification, and removal of features using elevation difference threshold for DTM generation.	Buildings, Vehicles, Vegetation	97% success rate when removing features. Works in both urban and mountainous areas.	[48]
Lidar-based Hazard Avoidance for Safe Landing on Mars	A. Johnson *Jet Propulsion Laboratory*	Hazard detection and avoidance for landing using the slope and terrain variation in LIDAR data as metric for landing safety.	Terrain, Rocks, Craters	Sensor requirements and successful simulation of landing on Martian surface.	[99]
Precise vehicle topology and road surface modeling derived from airborne LIDAR data	C. K. Toth *The Ohio State University*	Traffic monitoring, using extraction, classification, and velocity estimation of vehicles.	Vehicles, Roads	Vehicles are extracted and modeled to carry out the flow estimation.	[50]
Analysis of airborne laser-scanning system configurations for detecting airport obstructions	C. E. Parrish *University of Florida*	Study of ALS parameters for detection of small airport hazards. Extraction and classification of obstructions.	Small stationary objects such as signs and antennas.	An ALS title angle of no more than 20° and a flying height of 750m yields optimal detection.	[100]
Aerial Vehicle Navigation over Unknown Terrain Environments using Inertial Measurements and Dual Airborne Laser Scanners or Flash LADAR	A. Vadlamani *Ohio University*	Terrain referenced navigation using two airborne laser scanners	N/A	Successful navigation using two ALS to estimate and correct IMU errors such as drift.	[13]

Preliminary Design and Analysis of a LIDAR Based Obstacle Detection System	A. Vadlamani *Ohio University*	Method for ALS object detection and simulation.	Terrain features, airport obstructions	Optimal ALS parameters such as mounting angle, point density, and scanning speed have been analyzed. A simulator has been developed for LIDAR object detection on precision approach.	[6]
Applications of the robust interpolation from DTM determination	C. Briese *Vienna University of Technology (Austria)*	Algorithms for DTM generation with point cloud data.	Terrain	Successful elimination of non-terrain points from laser data.	[101]
Use of Large-Footprint Scanning Airborne LIDAR to Estimate Forest Stand Characteristics in the Western Cascades of Oregon	J. Means *Oregon State University*	Estimation of forest properties such as height, area, total biomass, and leaf biomass.	Forest, Trees	Detection of trees on steep slopes is difficult due to laser scatter.	[102]
Corridor navigation with a LIDAR/INS Kalman filter solution	W. Travis *Auburn University*	Navigation using data from low cost sensors in a Kalman filter.	Corridor walls	Successful navigation technique using post processing.	[53]
DTM extraction of LIDAR returns via adaptive processing	H. Lee *Mississippi State University*	Measuring terrain with removal of vegetation for DTM generation.	Terrain	Technique offers improved performance when measuring areas with steep slopes.	[103]